



## OPEN ACCESS

## EDITED BY

Ahmed M. Eldosouky,  
Suez University, Egypt

## REVIEWED BY

Amando P. E. Lasabuda,  
UiT The Arctic University of Norway,  
Norway  
Sayed Elkhateeb,  
South Valley University, Egypt

## \*CORRESPONDENCE

Sookwan Kim,  
✉ skwan@kiost.ac.kr

RECEIVED 04 June 2023

ACCEPTED 10 August 2023

PUBLISHED 25 August 2023

## CITATION

Kim S, De Santis L, Hong JK, Colizza E,  
Kim S, Bergamasco A, Lee S-H, Kang S-G,  
Lee MK, Kim H, Choi Y, Geniram A,  
Choi HG, Lee JI, Yoo K-C and Park Y  
(2023), Hunting paleoceanographic  
archives of ice sheet-ocean interaction in  
the northwestern Ross Sea, Antarctica.  
*Front. Earth Sci.* 11:1234347.  
doi: 10.3389/feart.2023.1234347

## COPYRIGHT

© 2023 Kim, De Santis, Hong, Colizza,  
Kim, Bergamasco, Lee, Kang, Lee, Kim,  
Choi, Geniram, Choi, Lee, Yoo and Park.  
This is an open-access article distributed  
under the terms of the [Creative  
Commons Attribution License \(CC BY\)](https://creativecommons.org/licenses/by/4.0/).  
The use, distribution or reproduction in  
other forums is permitted, provided the  
original author(s) and the copyright  
owner(s) are credited and that the original  
publication in this journal is cited, in  
accordance with accepted academic  
practice. No use, distribution or  
reproduction is permitted which does not  
comply with these terms.

# Hunting paleoceanographic archives of ice sheet-ocean interaction in the northwestern Ross Sea, Antarctica

Sookwan Kim<sup>1\*</sup>, Laura De Santis<sup>2</sup>, Jong Kuk Hong<sup>3</sup>, Ester Colizza<sup>4</sup>,  
Sunghan Kim<sup>3</sup>, Andrea Bergamasco<sup>5</sup>, Sang-Hoon Lee<sup>1</sup>,  
Seung-Goo Kang<sup>3</sup>, Min Kyung Lee<sup>3</sup>, Hyoungjun Kim<sup>3</sup>,  
Yeonjin Choi<sup>3</sup>, Andrea Geniram<sup>4</sup>, Hyoung Gyu Choi<sup>3</sup>, Jae Il Lee<sup>3</sup>,  
Kyu-Cheul Yoo<sup>3</sup> and Yongcheol Park<sup>3</sup>

<sup>1</sup>Korea Institute of Ocean Science and Technology, Busan, Republic of Korea, <sup>2</sup>National Institute of Oceanography and Applied Geophysics–OGS, Trieste, Italy, <sup>3</sup>Korea Polar Research Institute, Incheon, Republic of Korea, <sup>4</sup>Department of Mathematics and Geosciences, University of Trieste, Trieste, Italy, <sup>5</sup>Institute of Marine Sciences–National Research Council, Venice, Italy

The analysis of sedimentary deposits influenced by bottom currents in glaciated continental margins provides crucial insights into paleo-depositional and oceanographic conditions. These reconstructions enable the assessment of interactions between advance and retreat of grounded ice sheets and past ocean circulation patterns. However, questions regarding these interactions and their specific mechanisms remain largely unanswered due to a lack of data in this remote area. In this study, we conducted a comprehensive analysis by integrating marine geophysical data, surficial sediment cores, oceanographic measurements, and ocean circulation models. Our aim was to understand spatial and temporal variations in sedimentary and oceanographic conditions during the past glacial and interglacial periods in combination with the long-term stratigraphic evolution. By integrating and cross-referencing diverse datasets, we were able to infer how bottom-current-controlled deposits (i.e., contourites) developed along the western bathymetric high of the Central Basin in the northwestern Ross Sea margin, Antarctica. Contouritic deposits lying over and along the flanks of bathymetric highs were identified through their mound-shaped external geometry and acoustically stratified facies, characterized by reflectors pinching toward the moat. Acoustic facies and multi-beam backscatter results, in conjunction with sedimentary core data, revealed contrasting patterns. Bathymetric highs exhibited thin (<10 m thick) coarser-grained sedimentary layers with higher backscatter, while the lower slope and rise displayed thick (>10 m thick), finer-grained stratified sediments with lower backscatter. These findings indicate that seabed winnowing occurred by strong

**Abbreviations:** AABW, Antarctic Bottom Water; AASW, Antarctic Surface Water; ACC, Antarctic Circumpolar Current; ASC, Antarctic Slope Current; CDW, Circumpolar Deep Water; CMP, Common Mid-Point; DSW, Dense Shelf Water; GMRT, Global Multi-Resolution Topography synthesis; IBCSO, International Bathymetric Chart of the Southern Ocean; JOIDES, Joint Oceanographic Institutions for Deep Earth Sampling; KOPRI, Korea Polar Research Institute; LGM, Last Glacial Maximum; MBES, Multi-Beam Echosounder; MCS, Multi-Channel Seismic; ROMS, Regional Ocean Modeling System; RSU, Ross Sea Unconformity; SBP, Sub-Bottom Profiler; SCS, Single Channel Seismic; XCTD, Expandable Conductivity-Temperature-Depth.

bottom current during past glacial periods as supported by sedimentological analysis. The pathways of the westward-deflected dense shelf water outflow and the westward-flowing along-slope current, as simulated by oceanographic models, explain the distinctive development of contourites influenced by bottom-current processes. Moreover, the large accumulations of sediment in the contourites, resulting from bathymetric barriers in the north of the Central Basin, may contribute to submarine slope failures.

#### KEYWORDS

contourite, bottom current, Antarctica, Ross Sea, seismic stratigraphy, seafloor morphology

## 1 Introduction

The glaciated continental margins display geomorphic and sedimentary features that contain invaluable records, shedding light on variations in intensity and shifts in the locations of ocean bottom currents influenced by ice sheet dynamics (Rebesco et al., 1996; Dowdeswell et al., 2006; Uenzelmann-Neben, 2006; 2018; Pérez et al., 2015; Lasabuda et al., 2018; Le Heron et al., 2019; Rydningen et al., 2020; Mosher and Boggild, 2021; Bjordal-Olsen et al., 2023). Among these regions, the Ross Sea continental margin, positioned between East and West Antarctica, has evolved stratigraphically and geomorphologically over a long duration, shaped by the Antarctic Ice Sheet since the earliest Oligocene (Brancolini et al., 1995; De Santis et al., 1995; 1999; Bart and De

Santis, 2012; Anderson et al., 2014; Halberstadt et al., 2016; McKay et al., 2016; Bart et al., 2017). The Ross Sea plays a significant role in global ocean circulation by contributing cold and dense shelf water (DSW) through its outflow (Jacobs et al., 1970; Bergamasco et al., 2002; Budillon et al., 2002; 2011; Rivaro et al., 2003; Orsi and Wiederwohl, 2009). Additionally, the influx of warm Circumpolar Deep Water (CDW) and the westward-flowing Antarctic Slope Current (ASC) have been observed at the outer Ross Sea continental margin (Gordon et al., 2009; 2015; Smith et al., 2012; Carter et al., 2022) (Figure 1).

Given the close association between cryospheric and paleoceanographic changes in polar continental margins (Kennett, 1977; Uenzelmann-Neben and Gohl, 2012; Huang et al., 2014; Hochmuth et al., 2020; Kim et al., 2020), the outer

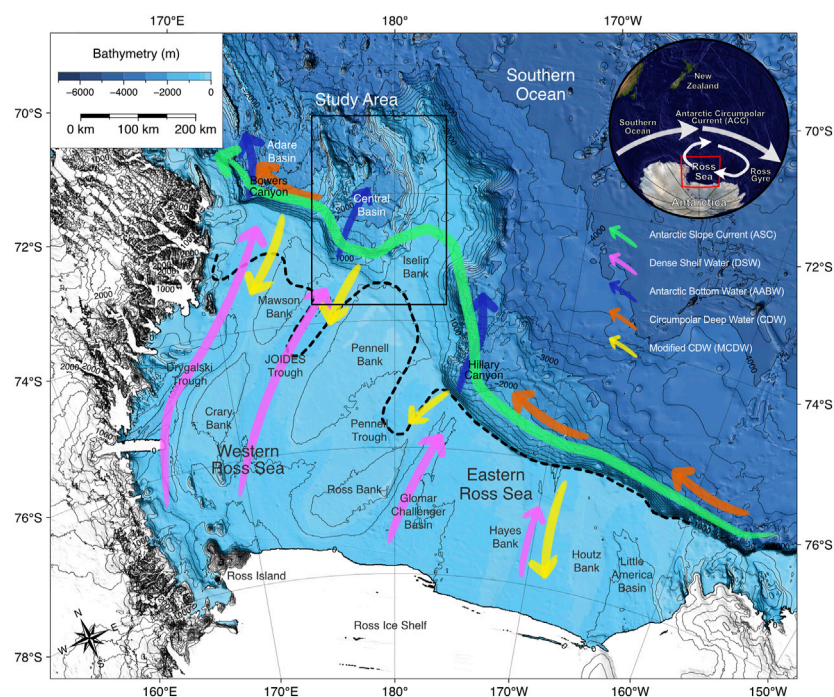


**FIGURE 1**

The regional bathymetry and elevation extracted from the International Bathymetric Chart of the Southern Ocean Version 2 (IBCSO v2; Dorschel et al., 2022) and oceanographic setting (modified from Smith et al., 2012) of Ross Sea region in Antarctica. The red rectangle in the upper right inset locates the Ross Sea in the Antarctica. In the upper right inset figure, the white thick and thin arrows represent the flow direction of the Antarctic Circumpolar Current (ACC) and the circulation of Ross Gyre, respectively. The black rectangle in the main figure locates the Central Basin. The main water masses in the Ross Sea are indicated by color-coded arrows, with labels and abbreviations provided in the upper right. The black dashed line is the reconstructed grounding line at the Last Glacial Maximum (Halberstadt et al., 2016).

continental margin of the Ross Sea is a key area for reconstructing the evolution of oceanographic and depositional conditions during the late Cenozoic, characterized by repeated ice-sheet advances and retreats. Despite the Ross Sea having a crucial influence on global ocean circulation through ocean–cryosphere interactions, our understanding of bottom-current-controlled sedimentary deposits (i.e., contourites) and the associated environmental conditions remains insufficient due to data limitations.

Previous seismostratigraphic studies in the Ross Sea embayment revealed the acoustic basement structure and stratal geometry affected by subglacial processes of grounded ice sheets, using single and multi-channel seismic (SCS and MCS) reflection profiles (Anderson and Bartek, 1992; Brancolini et al., 1995; De Santis et al., 1995; 1999; Bart and De Santis, 2012). However, recent acquisitions of SCS/MCS data and scientific drilling results (Granot et al., 2010; Gordon et al., 2015; Bart et al., 2017; Kim et al., 2018; McKay et al., 2019; Conte et al., 2021; Gales et al., 2021; King et al., 2022) have expanded our seismic coverage to the outer continental shelf, slope, and rise, enabling a better understanding of variations in depositional and oceanographic settings through continuous sedimentary records. Recent sedimentological studies in the northwestern Ross Sea have suggested that sedimentation on the continental slope is controlled by bottom-current activity coupled with DSW export and glacial meltwater pulses (Khim et al., 2021; Torricella et al., 2021; Bollen et al., 2022). Furthermore, strong bottom-current activity during glacial periods has been suggested through coarser sediment recovered from the Iselin Bank, which is an eastern boundary of the Central Basin (Kim et al., 2020).

Combining geomorphic and seismostratigraphic mapping results with sediment core data offers valuable insights into spatial variations in modern depositional and oceanographic environments, contourite development, and the reconstruction of past environmental settings (e.g., López-Quirós et al., 2020; Mosher and Boggild, 2021; Rodrigues et al., 2022). Bottom-current-controlled sedimentary processes along the continental slope can significantly impact sedimentation rates and slope stability, potentially leading to submarine landslides (Laberg and Camerlenghi, 2008; Miramontes et al., 2018). Therefore, understanding how bottom currents are influenced by climate change is crucial for assessing the potential risk of submarine geohazards (e.g., Gales et al., 2023).

This study focused on the Central Basin in the northwestern Ross Sea and mainly used seismic profiles and morpho-bathymetric data to identify bottom-current-controlled deposits. The primary objective was to understand the sedimentary and geomorphic processes that occurred in the Central Basin during previous glacial-interglacial periods. This investigation included the identification and mapping of acoustic facies of surficial sediments and seafloor morphology within the basin floor and surrounding bathymetric highs. The results of seabed mapping were compared with grain-size and water-content data extracted from sediment cores to validate the geophysical interpretations. Physical oceanographic measurements and ocean circulation models were used to assess the distributions of bottom-current features, the pathway and velocity of DSW cascading, and along-slope bottom currents under recent oceanographic conditions (e.g., Thran et al., 2018). This research can contribute to our comprehensive understanding of the environmental conditions

influencing the interplay between bottom currents and ice sheets in both modern and Quaternary periods, bridging the gap between paleoclimatic, paleo-oceanographic interpretations, and sparsely distributed sediment cores (McKay et al., 2019; Conte et al., 2021; King et al., 2022).

## 2 Regional setting

### 2.1 Geological and morphological setting

The Ross Sea continental shelf, which lies between  $\sim 70^{\circ}\text{S}$  and  $\sim 78^{\circ}\text{S}$  latitude and  $\sim 160^{\circ}\text{E}$  and  $\sim 150^{\circ}\text{W}$  longitude (Figure 1), consists of rift basins and half-grabens formed by the West Antarctic Rift System since the Early-mid Cretaceous (Lawver et al., 1992; Davey and Brancolini, 1995). The Joint Oceanographic Institutions for Deep Earth Sampling (JOIDES) Trough and Central Basin in the western Ross Sea were formed by a rifting episode that involved a NE–SW extension of  $\sim 100$  km, occurring from  $\sim 61$  to  $53$  Ma (Cande et al., 2000; Cande and Stock, 2004; Wilson and Luyendyk, 2009). A recent preliminary crustal model by marine gravity and seismic data suggests that the Central Basin was formed by the same extension episode with the JOIDES Trough (Davey et al., 2021). The Central Basin was actively infilled by sediments transported under a temperate climate in the early phase and wet-based glaciers since  $\sim 34$  Ma (Brancolini et al., 1995). In this study, the target sedimentary units are positioned above the Ross Sea Unconformity (RSU) 4 (middle Miocene,  $\sim 14.7$  Ma) (Savage and Ciesielski, 1983; Pérez et al., 2021) can be considered as post-rift sedimentary deposits and they developed in a relatively stable tectonic setting according to the tectonic history and stratigraphic evolution of the northwestern Ross Sea (Brancolini et al., 1995; Davey et al., 2021).

The JOIDES Trough, characterized by water depths of  $500$ – $600$  m in the outer shelf and  $600$ – $800$  m in the inner shelf, exhibits gently over-deepened (landward dipping) seafloor morphology (Figure 1). The JOIDES Trough is believed to have been one of the main drainage pathways of the East Antarctic Ice Sheet sourced ice feeding into the Ross Sea during the Last Glacial Maximum (LGM) (Anderson and Bartek, 1992; Shipp et al., 1999; Livingstone et al., 2012; Anderson et al., 2014; Harris et al., 2014; Halberstadt et al., 2016) and most of the glaciogenic sediment delivered to the Central Basin (Brancolini et al., 1995; Bart et al., 2000; Kim et al., 2018).

The Central Basin, located beyond the JOIDES Trough, is bounded to the east by the Iselin Bank, to the west by the Hallett Ridge, and to the north by the eastern branch of the Hallett Ridge named as Bank B (Kim et al., 2018) (Figure 2A). The regional bathymetry data show that a relatively gentle slope extending beyond the western part of JOIDES Trough mouth, characterized by an inclination of  $\sim 1.2^{\circ}$  within the water depth range of  $500$ – $1,400$  m. Subsequently, the middle to lower slope exhibits a lesser inclination of  $\sim 0.7^{\circ}$  within the depth range of  $1,400$ – $2,000$  m. Finally, the Central Basin floor demonstrates a nearly flat topography, with a slight inclination of  $\sim 0.2^{\circ}$  from  $2,000$  to  $2,200$  m, representing the lower slope transitioning to the basin floor (Figure 2A). In contrast, the eastern continental slope beyond the JOIDES Trough features a bounding bathymetric high

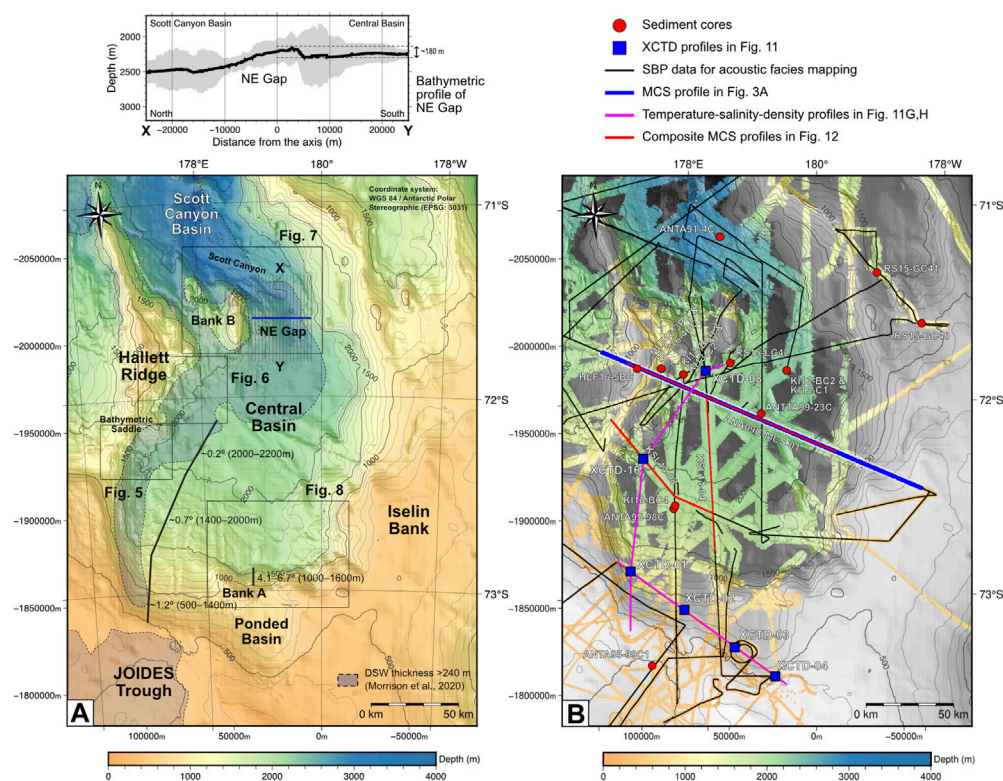


FIGURE 2

(A) Bathymetric map of the Central Basin extracted from IBCSO v2 (Dorschel et al., 2022). The thick black solid line with numbers represents the measured slope gradient beyond the JOIDES Trough. Blue translucent areas with dashed outlines indicate the distribution of dense shelf water (DSW) outflow thicker than 240 m, as given in the oceanographic modeling of Morrison et al. (2020). Black rectangles locate enlarged MBES bathymetry and backscatter images (Figures 5–8). The upper left inset is a median stacked bathymetric profile at the northeastern gap (NE Gap) of the Central Basin. The black solid line shows a stacked bathymetric profile and the gray area representing the  $2\sigma$  confidence bounds on the stacked median profile. (B) Map showing locations of sub-bottom profiler (SBP) and multi-channel seismic (MCS) data, multi-beam echosounder (MBES) bathymetry, sediment core sites, and expandable conductivity-temperature-depth (XCTD) data in the Central Basin and over its surrounding bathymetric highs. The MBES bathymetry data (color-coded grid) is superimposed on the regional bathymetry of IBCSO v2 (gray-color grid).

named as Bank A (Kim et al., 2018), which is associated with a steeper gradient ranging  $\sim 4.1^\circ$ – $6.7^\circ$  between 1,000 and 1,600 m (Figure 2A). Unlike the deeply incised submarine canyons observed at the Pennell and Glomar Challenger Trough mouths in the eastern Ross Sea (Hillary Canyon) and the western Ross Sea (Bowers Canyon), respectively, the gently sloping area beyond the mouth of the JOIDES Trough does not have any deeply incised submarine canyon (Figures 1, 2A). The Central Basin is connected to the deeper and smaller basin through a narrow gateway,  $\sim 30$  km wide, referred to informally as the Scott Canyon Basin and the northeastern gap (NE Gap), respectively (Figure 2A). According to the International Bathymetric Chart of the Southern Ocean Version 2 (IBCSO v2; Dorschel et al., 2022), the average water depth reveals a relatively shallow bathymetry in the NE Gap. This area is  $\sim 180$  m higher than the adjacent Central Basin floor (upper left inset of Figure 2). The Scott Canyon, a deeply incised submarine canyon, extends from the NE Gap to the continental rise in the Scott Canyon Basin floor (Davey, 2004). In contrast to the Bowers and Hillary Canyons, which originate from the shelf edge and upper slope, respectively, the Scott Canyon exhibits unique characteristics in its distinctive positioning within the deeper environment of the continental rise.

## 2.2 Oceanographic setting

The Antarctic Circumpolar Current (ACC), which is the most prominent oceanographic feature in the Southern Ocean, flows eastward around Antarctica (Whitworth, 1988; Cunningham et al., 2003; Carter et al., 2022) (upper right inset of Figure 1). Located south of the ACC, the Ross Gyre is a clockwise circulation element influenced by the advance and retreat of the Antarctic ice sheets (Kennedy et al., 2015; Carter et al., 2022). The Ross Gyre can entrain the CDW to the Ross Sea outer continental margin (Orsi and Wiederwohl, 2009). The CDW transports heat and salt to the Ross Sea continental margin (Jacobs et al., 2002; Jacobs, 2004). In the Ross Sea, ASC is a bottom water current that is located further south of Ross Gyre. The ASC flows westward along the Antarctic margin slope, driven by the easterly polar winds (Chavanne et al., 2010; Armitage et al., 2018; Carter et al., 2022).

DSW forms on the continental shelf through brine rejection in the Drygalski and JOIDES Troughs in the western Ross Sea (Jacobs et al., 1985; Budillon et al., 2002; Gordon et al., 2009; 2015; Orsi and Wiederwohl, 2009; Budillon et al., 2011). DSW is also generated by heat loss in the eastern Ross Sea (Bergamasco et al., 2002; Rivano et al., 2003) (Figure 1). This dense water mixes with surrounding

waters and subsequently sinks to the bottom of the ocean, forming Antarctic Bottom Water (AABW) (Orsi and Wiederwohl, 2009).

## 3 Materials and methods

### 3.1 Reflection seismic data

A total of 5,400 L-km of sub-bottom profiler (SBP) data were acquired in the Central Basin region using the Kongsberg SBP120 system during three separate R/V *Araon* Antarctic Expeditions—ANA03B, ANA05B, and ANA09C—conducted in the years 2013, 2015, and 2019, respectively (Figure 2B). The SBP data were simultaneously recorded together with MCS surveys and during transits at variable ship speeds from 5 to 12 knots. The SBP data have a lateral sampling interval of ~2.6 m when the ship was travelling at 5 knots and with a ping rate of 1 s. A chirp pulse with a linearly swept frequency was used, with a frequency range of 2.5–7.0 kHz and a pulse length of 20 ms. This configuration allowed for a maximum vertical resolution of about 0.3 ms, equivalent to ~23 cm at a sound speed of 1,500 m/s. The depth of penetration of SBP signal varies depending on the subsurface characteristics, such as lithology and physical properties. In most cases, it ranges from tens of meters to less than 100 m.

The original data recorded in the Topas Raw format were converted to the SEG-Y format to enable conventional seismic data processing. This processing included gain correction, delay time-shifting, and signal enveloping. These tasks were performed using the Seismic Unix software (<https://wiki.seismic-unix.org>).

During the ANA09C expedition in 2019, a basin-crossing MCS profile, ANA09C-MCS-01, was acquired to fill a gap in the existing MCS grid in the Central Basin (Figure 2B). The MCS data were acquired using eight airguns, specifically the Sercel G-Gun II, which had a combined volume of 1,200 in<sup>3</sup> and operated at a working pressure of 2000 psi. To ensure appropriate data coverage, the shot point interval was set at 50 m. A 1.5 km-long 120-channel solid-type streamer (Sercel Sentinel) was towed at a depth of 6 m below sea level during the MCS data acquisition. The MCS data were recorded with a length of 10 s and a sampling rate of 1 ms. Considering the shot interval and streamer geometry, each common mid-point (CMP) gather in the dataset provided a 15-fold coverage and featured a CMP spacing of 6.25 m.

The ANA09C MCS data underwent a standard seismic data processing workflow, using Schlumberger OMEGA 2017 software, which included deconvolution, trace editing, multiple attenuations, velocity analysis, and Kirchhoff pre-stack time migration. The resulting processed seismic profiles from ANA09C were combined with the existing MCS datasets (KSL12 in 2013 and KSL14 in 2015) sourced from the Korea Polar Data Center (KPDC, <https://kpdc.kopri.re.kr>) of the Korea Polar Research Institute (KOPRI) and legacy seismic data from the Antarctic Seismic Data Library System (SDLS, <https://sdls.ogs.trieste.it>). This compilation of the seismic dataset allowed the extension of previous seismic stratigraphic interpretations in the northwestern Ross Sea outer continental margin (Brancolini et al., 1995; Granot et al., 2010; Kim et al., 2018) into the ANA09C MCS data in the Central Basin region.

The processed SBP and MCS data were imported into Schlumberger Petrel software for seismic stratigraphic

interpretation and seismic facies mapping. The acoustic facies of the subsurface sediments, as delineated by the SBP data, were classified into two distinct types (Table 1): acoustically stratified (Facies S) and acoustically transparent (Facies T). This classification was based on an analysis of their internal configuration, external geometry, stacking patterns, and stratigraphic relationships (Veeken and van Moerkerken, 2013). The thickness of Facies S and Facies T for creating the isopach map was determined based on the penetration depth of the SBP data, which is influenced by the seabed morphology and geological conditions. Facies S can be further subdivided into two sub-types, namely, Facies Sh and Sw, based on the resolvable thickness, as outlined in Table 1. The resolvable depth of the SBP data provide a crucial information about the physical characteristics of the seafloor and the subsurface sedimentary layers, such as seafloor roughness (smooth vs. undulated), grain-size composition (finer vs. coarser), and sediment compaction (soft vs. hard) (e.g., Neto et al., 2013; Kim et al., 2021). Therefore, the thickness and distribution of these facies were mapped to show their spatial variability within the Central Basin and along the surrounding bathymetric highs.

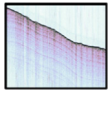
#### 3.1.1 Seismic stratigraphic framework

The seismostratigraphic unit boundaries of RSU4 (~14.7 Ma), RSU3-CB (~5.5–8.5 or ~10.5 Ma), and RSU2 (~2.8–4.0 or ~2.0 Ma) delineated in previous seismic stratigraphy and sediment core studies conducted on the western Ross Sea continental margin (Savage and Ciesielski, 1983; Brancolini et al., 1995; Granot et al., 2010; Bart et al., 2011; Kim et al., 2018; McKay et al., 2019; Pérez et al., 2021) were extended to the ANA09C-MCS-01 profile (Figure 3A). RSU1-CB (~0.7 Ma) cannot be correlated with deeper sedimentary layers due to its termination and merging with the seafloor reflection at the upper-mid slope beyond the JOIDES Trough mouth (Kim et al., 2018). However, establishing accurate correlations between the basin and bathymetric highs proved challenging. Therefore, the major unit boundaries were tentatively determined in the sedimentary deposits on the basement highs of the Hallett Ridge and western Iselin Bank, with consideration given to recent drilling results and seismostratigraphic findings from the eastern flank of the Iselin Bank (McKay et al., 2019; Conte et al., 2021).

### 3.2 Multibeam echosounder data

Simultaneous recording of multi-beam echosounder (MBES) bathymetry and backscatter data was conducted during the SBP and MCS surveys aboard the R/V *Araon*. The MBES data were processed using Caris HIPS and SIPS software and subsequently gridded at a lateral cell spacing of 50 m × 50 m using the *nearneighbor* module in GMT 6.3 software. The recently acquired MBES grid was then integrated with existing datasets from the IT17RS expedition by the RV OGS *Explora* in 2017 and the Global Multi-Resolution Topography synthesis (GMRT; Ryan et al., 2009). The GMRT data provides a maximum lateral resolution of ~61 m. The compilation of MBES bathymetry data encompasses ~40% of the Central Basin and its surrounding banks (Figure 2B). To address data gaps, the IBCSO v2 regional bathymetric data (Dorschel et al., 2022), with a resolution of 500 m × 500 m, were incorporated to fill in data gaps.

TABLE 1 Classification of acoustic facies of the surficial sedimentary strata in the sub-bottom profiler (SBP) data.

Seismic facies	Description	Interpretation	Occurrence	
Facies S		Thick (>10 m), highly stratified units with laterally continuous, low-to-medium amplitude subparallel internal reflections; weak-to-moderate amplitude seafloor reflection	Contourite deposits affected by relatively slow-flowing downslope and along-slope bottom-current processes in deep water settings; hemipelagic settling or suspension settling from turbid meltwater plumes in the ice-distal environments	Mid-lower slope of western Hallett Ridge, northern and eastern part of the Central Basin, on the Scott Canyon Basin, southwestern part of the Central Basin
Facies Sh		Thin (<10 m), weakly stratified units composed of most internal reflections with low amplitude and a few high-amplitude reflections; high amplitude seafloor reflection	Contourite deposits affected by bottom current winnowing processes in shallow water settings	Crests and upper slopes of the Hallett Ridge, northern and eastern slope of Iselin Bank
Facies Sw		acoustically transparent unit with erosional lower boundary and irregular- or lens-shaped external geometry	Subglacial till or glaciogenic debris flow deposits in the subglacial or ice-proximal settings; mass transport deposits in the deep water and ice-distal settings	Outer shelf and slope beyond the JOIDES Trough, eastern lower slope of the Hallett Ridge

The MBES backscatter data encompass the seafloor extending from the outer shelf and slope beyond the JOIDES Trough to the Central Basin and the surrounding bathymetric highs. To ensure accuracy, selections of the MBES backscatter data exhibiting poor quality (e.g., over the northern Iselin Bank and eastern Central Basin) were excluded.

### 3.3 Sediment core data

During the ANA03B and ANA05B expeditions, sediment core samples were retrieved from the northern part of the Central Basin (KI13-BC2, KI13-C1, and RS15-LC42), the northeastern flank of Hallett Ridge (KI13-BC3 and KI13-C2), the lower slope beyond the JOIDES Trough (KI13-BC4), and the northern tip of the Iselin Bank (RS15-GC40 and RS15GC41) (Figure 2B; Table 2). Additionally, as part of the Italian Antarctic Research Program (PNRA) expedition in 2016, a 240-cm-long piston core (HLF16-3PC) and two 27-cm-long box cores (HLF16-4BC and HLF16-5BC) were recovered from the crest and upper slope of Hallett Ridge. To encompass a wide range of depositional environments, four legacy sediment cores (ANTA91-4C, ANTA95-98C, ANTA95-99C1, and ANTA99-23C) collected during previous PNRA programs were also re-analyzed. Details regarding the sediment cores used in this study, such as location and recovered length, can be found in Table 2 and are further described in relevant studies (Tolotti et al., 2013; Ohneiser et al., 2019; Kim et al., 2020; Khim et al., 2021; Melis et al., 2021; Torricella et al., 2021; Bollen et al., 2022; McKay et al., 2022), as well as the Museo Nazionale dell'Antartide (<http://www.mna.it>) and the Italian Antarctic Data Center (<https://iandc.pnra.aq>).

Sediment grain sizes were derived using a laser diffraction instrument (Malvern Mastersizer) at multiple institutions: RS15-GC40 and RS15-GC41 were analyzed at KOPRI, RS15-LC40 at Victoria University of Wellington, and HLF16, ANTA91, ANTA95, ANTA99, and KI13 cores at the University of Trieste. Sediments with grain sizes larger than 2 mm were removed through sieving. For particles smaller than 2 mm, laser particle size analysis was conducted at intervals of 1 cm (KI13-BC2, KI13-BC3, KI13-BC4,

and HLF16-5BC) or 2 cm (HLF16-4BC) for box core samples, at intervals of 2, 4, 6, or 8 cm for gravity core samples (KI13-C1, KI13-C2, HLF16-3PC, ANTA95-98C, ANTA95-99C1, RS15-GC40, RS15-GC41), at 10 cm intervals for a jumbo gravity core (RS15-LC42), and ~20 or 30 cm intervals for the legacy cores (ANTA91-4C and ANTA99-23C). The sand (>63 μm), silt (63–2 μm), and clay (<2 μm) fractions were determined using the grain-size classification of Friedman and Sanders (1978) and Blott and Pye (2001).

The water content (WC) was calculated using the following equation, assuming a seawater salinity of 0.035 (Kim et al., 2020):

$$WC (\%) = (\text{mass of wet sediment} - \text{mass of dry sediment} + \text{mass of salt}) / \text{mass of wet sediment} \times 100$$

Water content values of the RS15 cores were calculated at KOPRI, while all other cores were analyzed at the University of Trieste. Water content data for KI13-C2 is unavailable due to a poor state of preservation (Table 2).

### 3.4 General ocean circulation model and oceanographic measurements

The Regional Ocean Modeling System (ROMS; Shchepetkin and McWilliams, 2005) was used to simulate bottom current conditions in the northwestern Ross Sea, specifically the Central Basin, for two distinct periods: 15-year periods of Austral winter spanning from 1999 to 2013 and 15-year periods of Austral summer spanning from 2000 to 2014. The model's lateral resolution is 5 km by 5 km, while the vertical resolution varies according to water depth, with a vertical grid comprising 32 cells uniformly distributed across all depths (e.g., 50-m vertical resolution at 1,600 m water depth). In this study, the lowest layer of the model was used to depict the speed and direction of bottom currents, which play a significant role in influencing sedimentary processes.

The expandable conductivity-temperature-depth (XCTD) data collected during the ANA05B expedition in 2015 were used to produce potential temperature-salinity ( $\theta/S$ ) diagrams using the

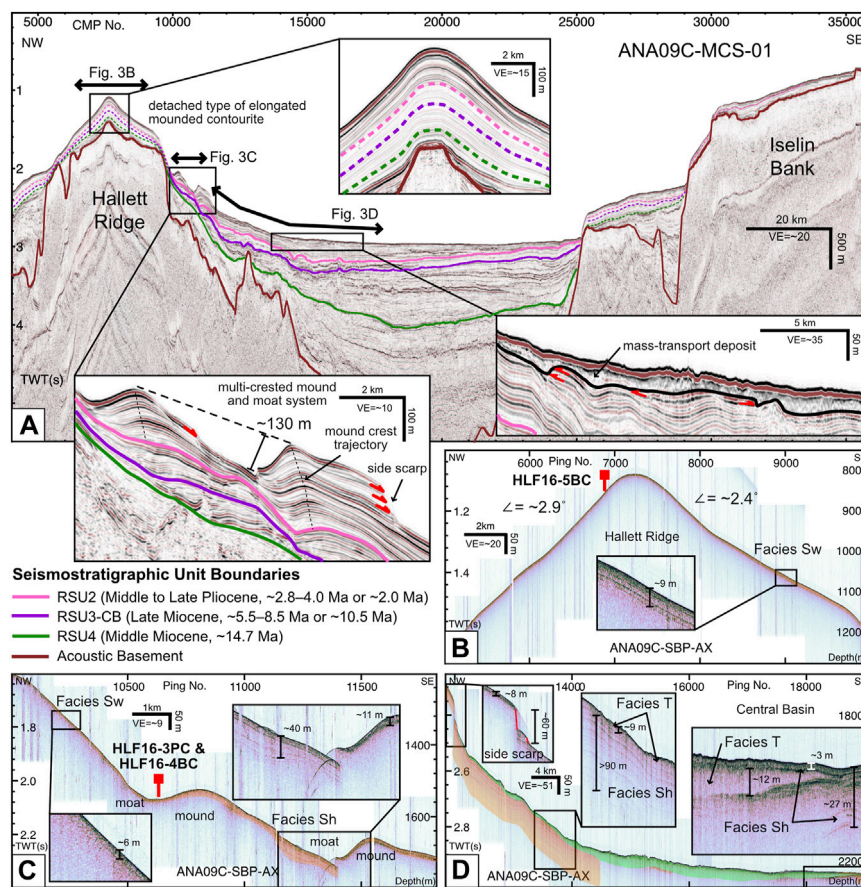


**FIGURE 3**

(A) The cross-basin multi-channel seismic (MCS) profile ANA09C-MCS-01, showing the acoustic basement structure and seismic stratigraphic setting in the Central Basin, Hallett Ridge, and Iselin Bank. Color-coded lines in the MCS profile indicate seismostratigraphic boundaries. Dashed lines in the sedimentary deposits on the basement highs of the Hallett Ridge and western Iselin Bank are tentatively identified seismostratigraphic boundaries. Black double arrows represent the locations of corresponding sub-bottom profiler (SBP) images shown in (B–D). Red arrows mark the termination of internal reflections against scarps, suggesting slope failures or erosional surfaces. (B) SBP image shows thin (<10 m) stratified sedimentary layer of Facies Sw (orange-shaded area) on the crest of Hallett Ridge. The red icon pointing down indicates a location of sediment core. (C) Thin stratified sedimentary layer on the upper slope and moats, thickening in the down-slope direction. (D) Thick stratified sedimentary layer of Facies Sh (orange-shaded area) on the lower slope of the western Central Basin, overlain by an irregular-shaped sediment body of Facies T (green-shaded area) in the northwestern part of the Central Basin.

Seawater 3.3 package in Python. These oceanographic measurements serve as valuable inputs to represent the contemporary thermohaline structure of the Central Basin region in this study.

## 4 Results

### 4.1 Seismic stratigraphic analysis

#### 4.1.1 MCS data

The basin-crossing MCS profile reveals that the Central Basin has filled with sediment layers reaching a thickness of ~2–3 km (Figure 3A). On the crest of the Hallett Ridge, there is a mounded sedimentary deposit with continuous internal reflections, ranging in thickness from 200 to 350 m (CMP No. 5500–9,500 in Figure 3A). Contrasting the eastern basement of the Hallett Ridge, which exhibits a series of tilted blocks, the western side of the Iselin

Bank features a broad bathymetric bench spanning ~23 km. This bathymetric bench is covered by sheet-like, stratified sediments without distinct mounded stacking patterns (CMP No. 25000–29000 in Figure 3A).

The deposition of small patches of sediments was initiated above RSU4 on the eastern slope of Hallett Ridge (CMP 10000–12000 in Figure 3A), and the undulated sedimentary deposits developed until the time of RSU2. Above RSU2, the subparallel internal reflections of the undulating sediments are more laterally continuous, and have distinctive trough and mound features on the slope. The crests of the small mound features exhibit a migration pattern towards higher elevations along the mid-lower slope of the Hallett Ridge (lower left inset of Figure 3A). Additionally, the seismostratigraphic unit above RSU2 is characterized by higher thickness than the underlying unit located between RSU2 and RSU3-CB, both on the lower slope of the northern Hallett Ridge and within the western part of the Central Basin (CMP 12000–17000 in Figure 3A).

TABLE 2 Sediment cores retrieved in the northwestern Ross Sea margin.

Expedition	Core name	Gear type	Year	Water depth (m)	Latitude	Longitude	Recovery (cm)	Average sand/silt/clay content (%)	Average water content (%)
ANA03B	KI13-BC2	Box	2013	2,246	71°52'S	179°30'E	37	17.8/76.3/5.9	37.3
ANA03B	KI13-C1	Gravity	2013	2,256	71°52'S	179°30'E	326	16.7/73.3/10.0	29.5
ANA03B	KI13-BC3	Box	2013	1,800	71°52'S	177°48'E	35	19.6/73.5/6.9	41.1
ANA03B	KI13-C2	Gravity	2013	1,797	71°52'S	177°48'E	232	31.2/62.3/6.5	-
ANA03B	KI13-BC4	Box	2013	1,772	72°34'S	177°33'E	44	14.1/79.2/6.7	41.1
ANA05B	RS15-GC40	Gravity	2015	1,083	71°37'S	178°17'W	257	65.2/32.9/1.8	23.9
ANA05B	RS15-GC41	Gravity	2015	1,557	71°23'S	178°59'W	540	30.2/64.9/5.0	34.4
ANA05B	RS15-LC42	Gravity	2015	2,084	71°49'S	178°35'E	1,186	16.3/79.8/3.9	36.3
PNRA	ANTA91-4C	Gravity	1991	2,815	71°10'S	178°28'E	630	13.3/75.2/11.5	36.6
PNRA	ANTA95-98C	Gravity	1995	1,788	72°33'S	177°34'E	376	11.4/75.5/13.1	27.7
PNRA	ANTA95-99C1	Gravity	1995	532	73°22'S	177°02'E	71	29.5/64.3/6.2	21.5
PNRA	ANTA99-23C	Gravity	1999	2,158	72°05'S	179°04'E	548	13.4/62.3/11.0	36.9
PNRA	HLF16-3PC	Piston	2016	1,320	71°50'S	177°26'E	240	44.3/51.3/4.4	25.5
PNRA	HLF16-4BC	Box	2016	1,320	71°50'S	177°26'E	26	41.0/52.3/6.7	23.6
PNRA	HLF16-5BC	Box	2016	800	71°50'S	177°03'E	26	49.9/46.0/4.1	25.8

Irregular-shaped sediment body, characterized by indistinct internal reflections, is evident in the shallow subsurface strata on the lower slope of the Hallett Ridge and in the northwestern portion of the Central Basin (CMP 12000–18000 in Figure 3A). The base of this sediment body truncates the underlying wavy, stratified sedimentary succession (lower right inset of Figure 3A).

#### 4.1.2 SBP data

The acoustically stratified facies (Facies S) is distinguished by its subparallel internal reflections, which align with the lower strata in a conformable manner. Within Facies S, a relatively thin sedimentary deposit (Facies Sw) exhibits a strong seafloor reflection and faint subparallel internal layers, less than 10 m in thickness at a sound speed of 1,500 m/s (Figure 3B; Table 1). On the other hand, a thicker deposit of Facies S (Facies Sh), surpassing 10 m in thickness, displays a weaker seafloor reflection and greater penetration depth (Figures 3C, D; Table 1). In contrast to Facies S, the acoustically transparent facies (Facies T) is identified by its poorly defined internal reflections and a lens-shaped or irregular external geometry (Table 1). Acoustically transparent subunits of Facies T exhibit lower boundaries that truncate the underlying strata, while their upper boundaries align subparallel to the internal reflections of the overlying stratified subunits (Figure 3D).

Isopach maps derived from the SBP data provide the spatial distribution and depocenters of Facies S and T (Figures 4A, B). Facies Sh, characterized by relatively thick and stratified subunits,

mainly developed along the mid-lower slope of the eastern flank of Hallett Ridge, the northeastern sector of the Central Basin floor, as well as the Scott Canyon Basin floor (orange to yellow areas in Figure 4A). Smaller patches of Facies Sh are observed on the lower slope of the southwestern part of the Central Basin facing the eastern slope of Hallett Ridge (red line labeled X–X' in Figure 4C). In contrast, the thinner stratified subunits of Facies Sw are primarily distributed along the crests and upper slopes of both the Hallett Ridge and Iselin Bank (Figures 3B, C, purple to navy-blue areas in Figure 4A). Additionally, Facies Sw can be found on the lower slope extending beyond the JOIDES Trough mouth and within the southern region of the Central Basin floor (Figure 4A).

Facies T occurs on the outer continental shelf and the gentle slope, extending beyond the JOIDES Trough mouth (Figure 4B). A notable occurrence within the northwestern sector of the Central Basin is the presence of a considerable deposit of Facies T, distinguished by its thickness surpassing 10 m (Figure 4B). This deposit has an estimated volume of ~9.7 km<sup>3</sup>.

#### 4.2 Multibeam bathymetry and backscatter intensity analyses

The MBES bathymetry grid obtained from the southwestern part of the Central Basin shows the presence of undulations oriented parallel to the lower slope of southern Hallett Ridge in deeper waters

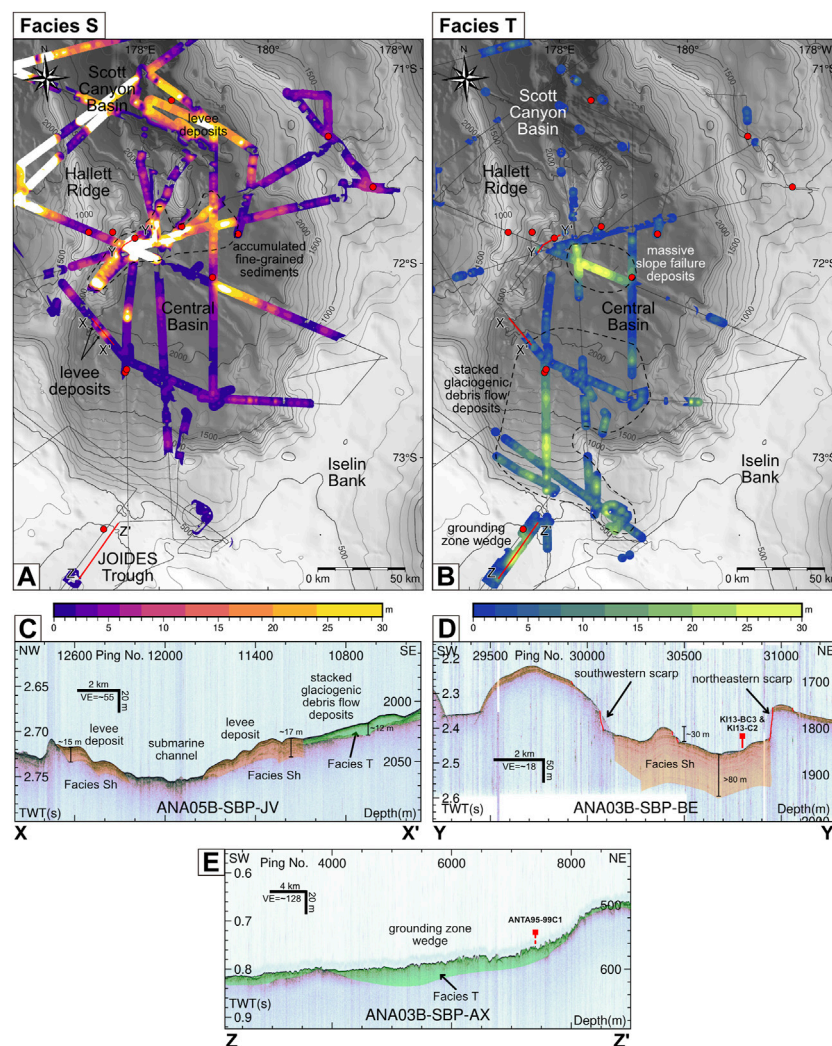


**FIGURE 4**

(A) Sediment thickness map showing acoustically stratified facies (Facies S) resolved from SBP data in the study area. Thin black lines represent the SBP data used for acoustic facies mapping. The red lines locate SBP profiles shown in (C, D). The red dots represent the locations of sediment cores used in this study (Figures 2, 9; Table 2). (B) Sediment thickness map showing acoustically transparent facies (Facies T). (C) The SBP profile imaging the presence of a submarine channel-levee feature in the southwestern part of the Central Basin. (D) The SBP profile displaying the side scarps of slope failures on the lower slope of northeastern Hallett Ridge. The red icon pointing down indicates a location of sediment core. (E) The SBP profile showing the grounding zone wedge on the outer shelf of the JOIDES Trough. The dashed red icon pointing down indicates a projected location of sediment core.

ranging from ~1700 to 1900 m. These undulations deviate the slope by crest amplitudes of ~45 and ~78 m (upper right inset of Figure 5A). The southern crest of Hallett Ridge near the JOIDES Trough mouth is asymmetric, with a slope gradient of ~2.1° towards the west and ~4.0° towards the east, extending from the crest at 1,000 m to the upper slope at 1,150 m (upper right inset of Figure 5B). On the crest of the Hallett Ridge, high backscatter intensities are observed, while the elongated mounds parallel to the slope exhibit varying intensities ranging from moderate to high (Figure 5B). The low backscatter stripes observed near the undulations (Figure 5B) exhibit a notable association with the 40-m-deep trough and mound features (Figures 4A, C).

Furthermore, the MBES data acquired from the northeastern Hallett Ridge region show a trapezoid-shaped bathymetric depression with an area of >220 km<sup>2</sup> on the middle to lower slope (Figure 6). The depression is almost flat and is bounded by

scarps measuring ~12 km in length towards the southwest and ~18 km in length towards the northeast (Figure 6B). These scarps displayed a relief ranging from ~40 to 50 m (Figure 4D). The backscatter intensity within this depression generally remains at a low to moderate level compared to the crest and upper slope of the Hallett Ridge (Figure 6B). At the downslope end of the northeastern scarp, wrinkled or hummocky seafloor features are observed, exhibiting moderate to high backscatter intensities in comparison to the low backscatter levels observed in the surrounding flat morphology (purple dashed ellipses in the right inset of Figure 6B).

The southern part of Hallett Ridge is asymmetric (Figure 5), becoming more symmetric towards the northern part (Figures 3A, B, 6A). The slope gradient in this region measures ~2.9° towards the west and ~2.4° towards the east, extending from the crest to the

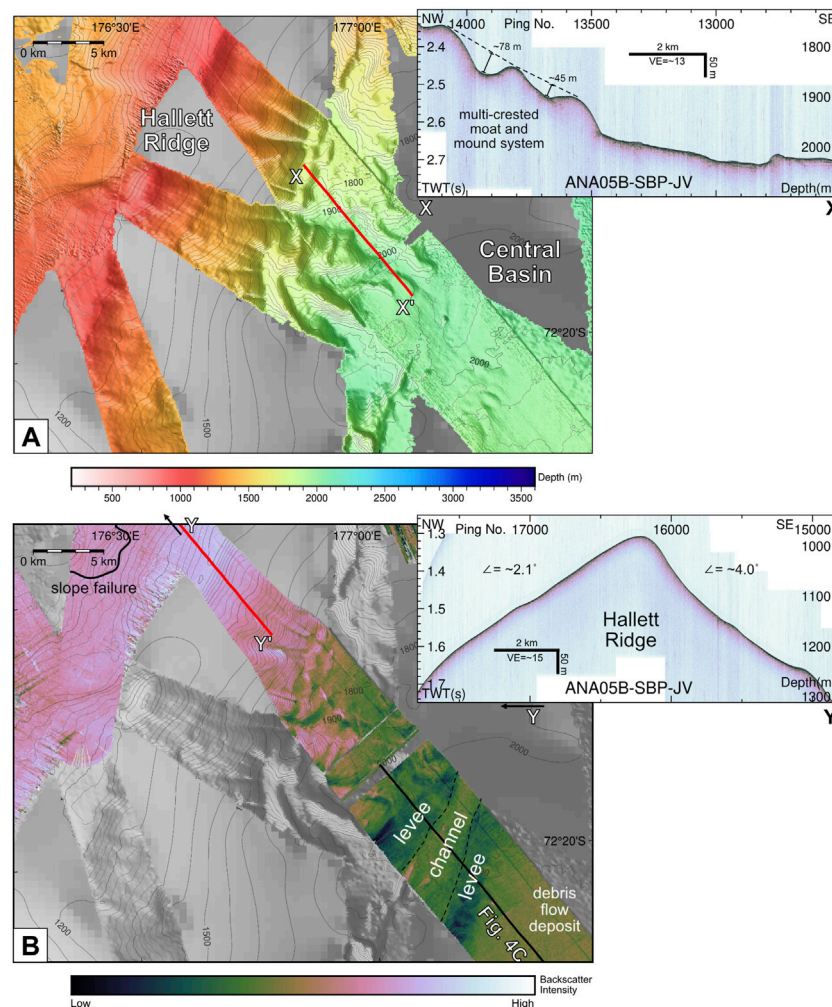


**FIGURE 5**  
**(A)** Detailed submarine morphology of the southeastern Hallett Ridge and the western part of the Central Basin captured in an enlarged mosaic of MBES bathymetric data. The red line locates of the SBP data shown in the upper right inset. **(B)** MBES backscatter data illustrating high and low backscatter intensities depicted in bright and dark green colors, respectively.

upper slope. Higher backscatter intensities are observed on the northern crest of the Hallett Ridge, while the northwestern Central Basin floor displays relatively lower intensities (Figure 6B).

Similar to the southwestern portion of the Central Basin, the northern part of the eastern flank of the Hallett Ridge displays slope-parallel elongated seafloor undulations at ~1,300–1850 m (Figure 6A). Additionally, the subsurface stratal patterns of these undulations can be observed in the MCS (Figure 3A) and SBP data (Figure 3C). The northward-elongated undulations with a crest amplitude of ~130 m (lower left inset of Figure 3A) exhibit moderate to low backscatter intensities (Figure 6B).

The Scott Canyon, developed north of Bank B, exhibits deep incisions exceeding 100 m in depth, initiating at ~2,200 m from the NE Gap of the Central Basin (Figure 7). This canyon features a sinuous thalweg that extends in a northwestward direction, characterized by side-scarps. However, the thalweg becomes unclear at ~3,300 m in the northern region of the Scott Canyon Basin (Figure 7A). The northeastern levee of the Scott Canyon shows a relatively smooth seafloor (upper right inset of Figure 7A)

characterized by low backscatter intensity (Figure 7B). In contrast, the southwestern part of the levee displays a relatively steeper morphology, facing the northern slope of Bank B (Figure 7A). Bank B stands over 1,500 m higher than the northern Central Basin floor, is separated from the western side of the Iselin Bank by the NE Gap (Figures 2, 7). Small conical-shaped mounds are observed around the 1500-m-high mount (purple dashed ellipses in Figure 7B). The bathymetric high located between the Hallett Ridge and Bank B displays linear seafloor features trending in a SE–NW or SSE–NNW direction (Figure 7A) with moderate to high backscatter intensity (Figure 7B).

The southeastern region of the Central Basin is bounded by a relatively steep slope of Bank A and the southwestern side of the Iselin Bank (Figure 8). Small conical-shaped mounds can be observed in front of the steep slopes of Bank A and the western slope of the Iselin Bank, exhibiting small-scale slope failures similar to those found along the fringe of Bank B. Additionally, distinctive downslope incisions are apparent on the southwestern slope of Iselin Bank (Figure 8A). Moderate intensities are present over the stacked

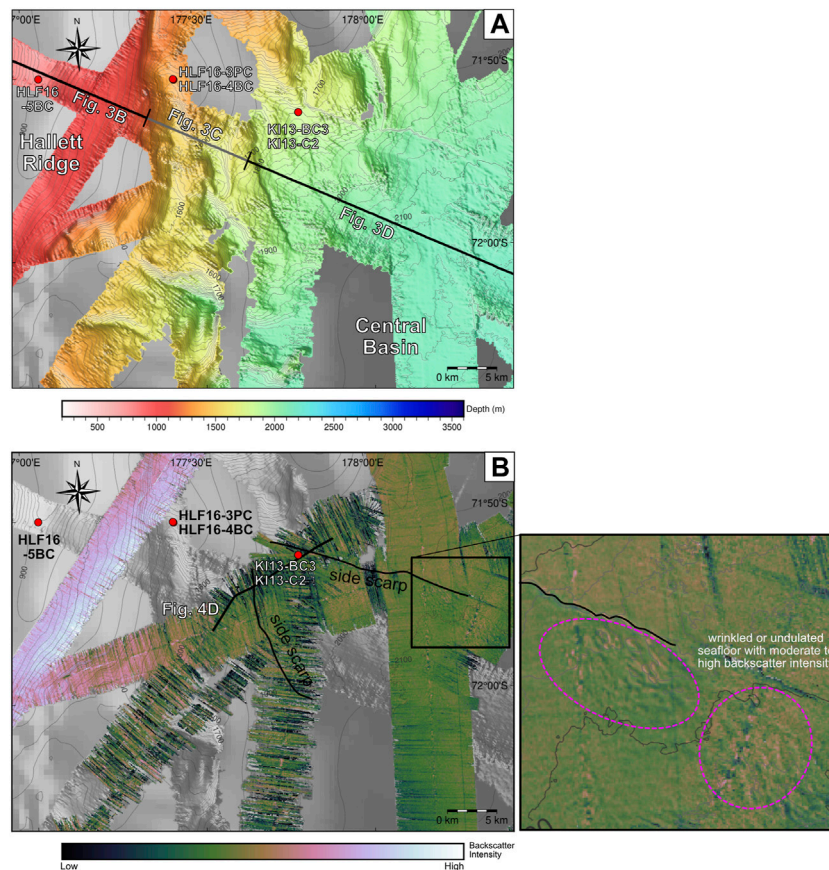


**FIGURE 6**

(A) Enlarged mosaic of the MBES bathymetry showing the northwestern sector of the Central Basin. Black and gray lines locate the SBP data crossing eastern slope of Hallett Ridge and northwestern part of Central Basin (Figures 3B–D). The red dots represent the locations of sediment cores. (B) MBES backscatter data of the northwestern sector of the Central Basin. Relatively moderate to high backscatter intensities observed on the wrinkled or undulated seafloor features in front of northern side scarp of the slope failure feature. The black line locates the SBP data crossing the slope failure feature (Figure 4D).

acoustically transparent lenses (Facies T) and stratified surficial sedimentary layer (Facies Sw) located on the southern portion of the Central Basin floor (lower right inset of Figures 8A, B). There is no distinctive difference in backscatter intensity between the top of Facies T and Facies Sw. Meanwhile, higher backscatter intensities are observed on the bathymetric high of Bank A and on the top of small conical mounds (purple dashed ellipses in Figure 8B).

### 4.3 Grain-size and water-content analyses of surficial sediments

Sediment cores were acquired from the crest and upper slope of bounding bathymetric highs, as well as the middle to lower slope and the Central Basin floor (Figure 9; Table 2). Longer sediment cores were collected in the lower slope and basin floor regions than in the upper slope and crests of bathymetric highs (Figure 9; Table 2).

Box core HLF16-5BC was retrieved from the crest of Hallett Ridge, measuring 26 cm in length. This core has an average sand content of 49.9%. Another box core, HLF16-4BC, also 26 cm in length and collected from Hallett Ridge, exhibits an average sand content of 41.0%. Additionally, a piston core, HLF16-3PC,

extending to a length of 240 cm on Hallett Ridge, displays a sand content 44.3% (Table 2). Core RS15-GC40 on the northern shallow region of the Iselin Bank exhibits an average sand content of 65.2%. On the outer shelf of the JOIDES Trough, core ANTA95-99C1, measuring 71 cm in length, shows an average sand content of 29.5%. This core is characterized by a relatively shallow penetration depth, distinguishing it from other piston or gravity cores. The mean water contents of HLF16-3PC, HLF16-4BC, HLF16-5BC, RS15-GC40, and ANTA95-99C1 range from 21.5% to 25.8% (Table 2).

In contrast, sediment cores collected from deeper areas generally exhibit lower average sand content values. The 35-cm-long box core, KI13-BC3 and the 232-cm-long gravity core, KI13-C2, exhibit lower average sand contents of 19.6% and 31.2%, respectively. Similarly, the 1186-cm-long gravity core, RS15-LC42, displays a low average sand content of 16.1%. Core ANTA99-23C shows an average sand content of 13.4% over its 548 cm length. On the mid-slope and small basin of the northern Iselin Bank, core RS15-GC41, displays an average sand content of 30.2%. The remaining cores, obtained at greater depths, exhibit average sand content ranging from 11.4% to 17.8% (KI13-BC4: 14.1%, KI13-C1: 16.7%, KI13-BC2: 17.8%, ANTA91-4C: 13.3%, and ANTA95-98C: 11.4%). Regarding water content, the majority of sediment cores retrieved from the mid-

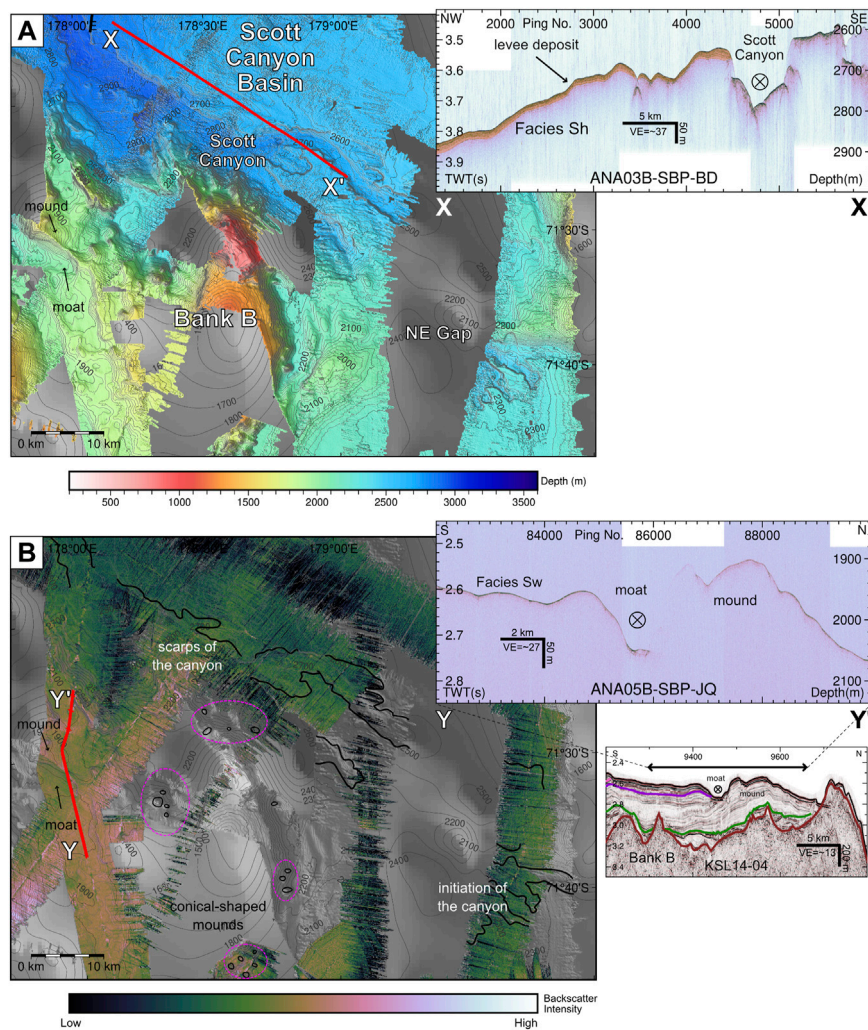


**FIGURE 7**

(A) Enlarged mosaic of the MBES bathymetry showing the northern sector of the Central Basin including Bank B, northeastern gap, and Scott Canyon Basin. The red line indicates the locations of the SBP data shown in the upper right inset. (B) Corresponding MBES backscatter data. The purple dashed ellipses indicate groups of small conical-shaped mounds. The SBP profile, depicted in the upper right inset, illustrates the shallow subsurface strata of contourites on Bank B. The MCS profile, corresponding to the SBP data (black double arrow in the right inset), illustrates the subsurface seismostratigraphic units and acoustic basement of Bank B (modified from Kim et al., 2018).

lower slope and basin floor exhibit high average water contents, surpassing 30%, with some cores even exceeding 40% (KI13-BC3 and KI13-BC4). However, two cores, ANTA95-98C (27.7%) and KI13-C1 (29.5%), deviate slightly with relatively lower water content less than 30%. Nevertheless, these two cores still exhibit higher water content in comparison to the sediment cores obtained from shallower depths.

#### 4.4 Oceanographic measurements and circulation model

The 15-year mean of ROMS ocean circulation models for austral winters (1999–2013) and summers (2000–2014) shows a clockwise circulation of bottom current flow in the Central Basin (Figures 10A, B). The model predictions suggest both flow speed and direction were similar for austral winters and summers, with slightly higher

speeds observed during the austral summer. However, the difference in speed between the two seasons is relatively small.

On the upper slope, seaward of the JOIDES Trough mouth, a faster westward-flowing bottom current stream is observed parallel to the shelf edge at water depths ranging from 400 to 800 m, with an average speed of 15 cm/s. Certain areas within it exhibit velocities exceeding 20 cm/s (Figures 10A, B). The eastern flank of southern Hallett Ridge, at water depths of ~1,300–1900 m, is characterized by a northward branch of the bottom current stream, with speeds ranging from 15 to 20 cm/s. The northward flow along the northeastern flank of Hallett Ridge and the southern slope of Bank B slows down to speeds of 8–15 cm/s. As the current flows around Bank B to the west of the NE Gap, its velocity increases to ~20 cm/s. In contrast, the bottom along the western flank of Iselin Bank is characterized by a contour-parallel southward flow with speeds ranging from 8 to 15 cm/s, and in some areas exceeding 15 cm/s. This southward flow contributes to a clockwise circulation

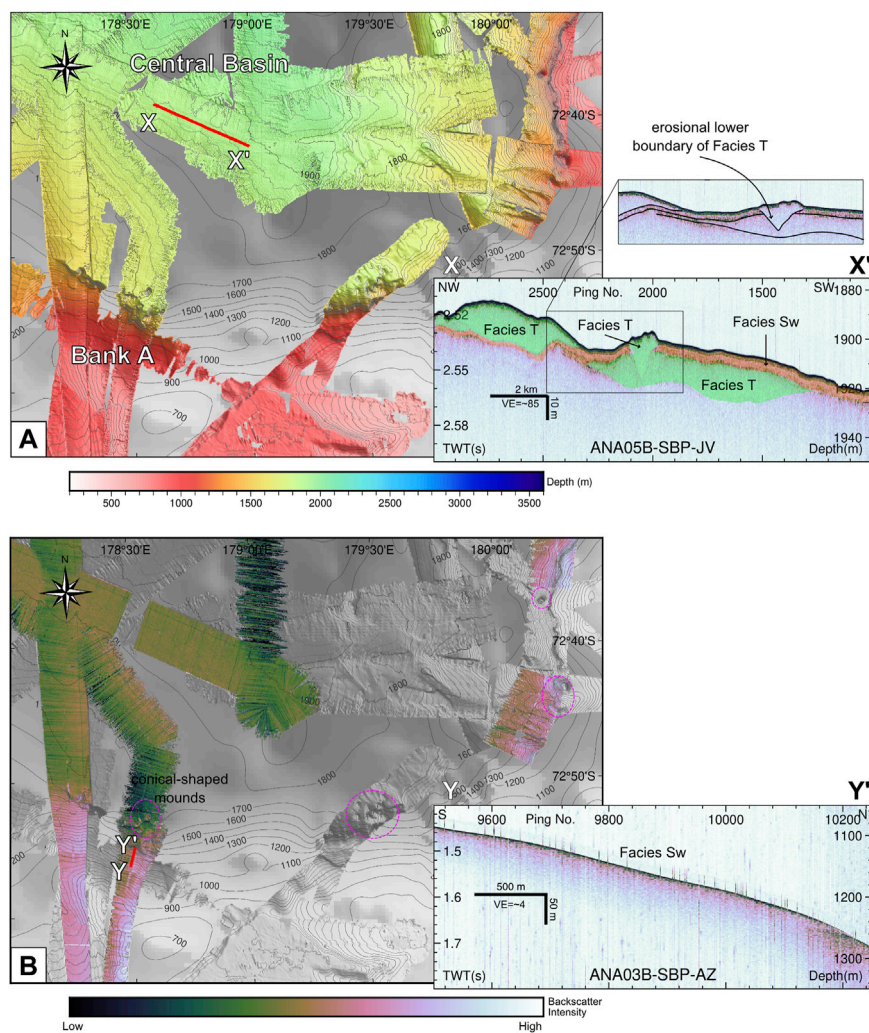


**FIGURE 8**

(A) Enlarged mosaic of the MBES bathymetry showing the southeastern sector of the Central Basin. The red line indicates the locations of the SBP data shown in the lower right inset. (B) Corresponding MBES backscatter data.

within the Central Basin. On the other hand, the crests of the northern Hallett Ridge and Iselin Bank exhibit very slow bottom current speeds, estimated to be less than 5 cm/s based on the circulation models.

The annual variabilities of bottom current speed of austral winter and summer are generally pronounced along the slopes of the surrounding bathymetric highs as indicated by the standard deviation (Figures 10C, D). In contrast, it is comparatively lower in the central section of the basin, the shallow region of the south Iselin Bank, and the northern crest of Hallett Ridge. The distribution of high standard deviation values (>2 cm/s) of the bottom current speeds shows a similar trend to the distribution of moderate to fast-flowing (>8 cm/s) along-slope currents. Significant levels of variability (>5 cm/s) are observed along the southeastern slope of the Hallett Ridge, especially during the austral winter (Figure 10C).

The analysis of XCTD data reveals the presence of three distinct water masses within the Central Basin (Figures 11A–F). These water masses comprise the cold and fresh surface water (Antarctic Surface Water: AASW), the less cold and salty deep water (CDW), and the

cold and dense bottom water (DSW). This is evident from the temperature-salinity-density profiles obtained by obliquely crossing the mid-slope to the outer shelf beyond the JOIDES Trough mouth (Figure 11G). Additionally, the XCTD data collected in the deeper water depths along the southern and northern slopes of Hallett Ridge demonstrate the extension of cold and dense bottom water further northward (Figures 11E, F, H).

## 5 Interpretation and discussion

### 5.1 Bottom-current-controlled sedimentary architecture in MCS data

The large mound deposit developed on the crest of Hallett Ridge (Figure 3A) can be interpreted as a detached-type of elongated, mounded contourite influenced by along-slope bottom currents based on its geometric and acoustic characteristics (Rebesco et al., 2014; Rodrigues et al., 2022). The presence of the similar

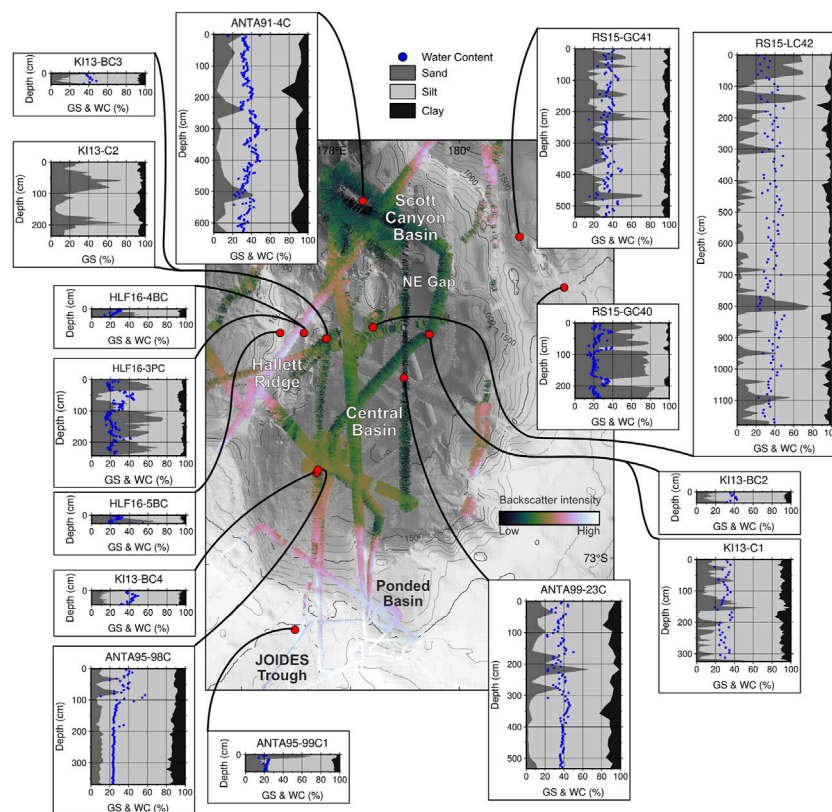


**FIGURE 9**

Grain size (GS) and water content (WC) analysis of all sediment cores in the Central Basin. Dark gray, light gray, and black indicate sand, silt, and clay contents of the surficial sediments, respectively. Blue dots are water content values in the sediment cores. The color-coded grid indicates MBES backscatter intensity. Red dots are the locations of the sediment cores.

scale sedimentary deposit, as reported in a previous study on the southern Hallett Ridge (Kim et al., 2018) (KSL14-08 in Figure 12), indicates that the mound likely extends along the Hallett Ridge. The asymmetric stacking pattern of the mound on the southern Hallett Ridge, characterized by a thinner stratified unit above RSU2 on its steeper eastern flank, can be attributed to the influence of fast-flowing bottom currents (Figure 12). Moreover, the relatively low topography of a saddle-like feature (Figure 2A) serves as a preferred pathway for the along-slope bottom current, allowing it to flow towards the Adare Basin when encountering the bathymetric barrier presented by the crest of Hallett Ridge. The concentrated and fast-flowing bottom current passing through the saddle of the southern Hallett Ridge contributes to an asymmetric stacking pattern and external morphology. The contouritic mound in the northern sector of Hallett Ridge displays a more symmetrical, aggradational stacking pattern in comparison with the one in the southern sector (Figures 3A, 12). This implies that the along-slope current weakens farther north, creating a less energetic and more uniform environment on both flanks of Hallett Ridge, consistent with the model of modern bottom current circulation (Figures 10A, B).

The elongated and parallel undulating sedimentary features along the northeastern slope contour of Hallett Ridge (Figures 3A, C, 6A) are interpreted as a multi-crested mound-and-moat system. This interpretation is consistent with previous work in this region (Kim et al., 2018) (Figure 5A) and is supported by analogies

drawn from similar features observed in other regions (Howe et al., 2002; Lu et al., 2003; Verdicchio and Trincardi, 2008; Martorelli et al., 2011; García et al., 2016; Miramontes et al., 2016). We interpret the long-term development of these elongated features as suggesting that the currents have persisted throughout their development with similar magnitudes to today. The migration pattern of internal reflectors (lower left inset of Figure 3A), which show an up-slope migration and onlap onto older reflectors within the multi-crested mound, further supports the influence of slope-parallel bottom currents in the formation of these features. This migration pattern distinguishes them from deformations caused by soft-sediment mechanisms such as creep folds, which lack true lateral migration (e.g., up-slope or up-current movement) and exhibit broader crests and narrower troughs (Wynn and Stow, 2002 and references therein).

The thicker development of the multi-crested mounds since the middle to late Pliocene (above RSU2), which formed over a shorter period (~4.0 Myr) compared to the underlying depositional layers between RSU4 to RSU2 (lower left inset of Figure 3A), indicates a higher influx of sediment towards the north than the previous period during the middle Miocene to middle Pliocene (~10.0 Myr). This interpretation, based on a single 2-D seismic profile, is consistent with previous regional sediment thickness mapping results in the Central Basin (Kim et al., 2018), which revealed a distinct depocenter along the northeastern lower slope of Hallett Ridge

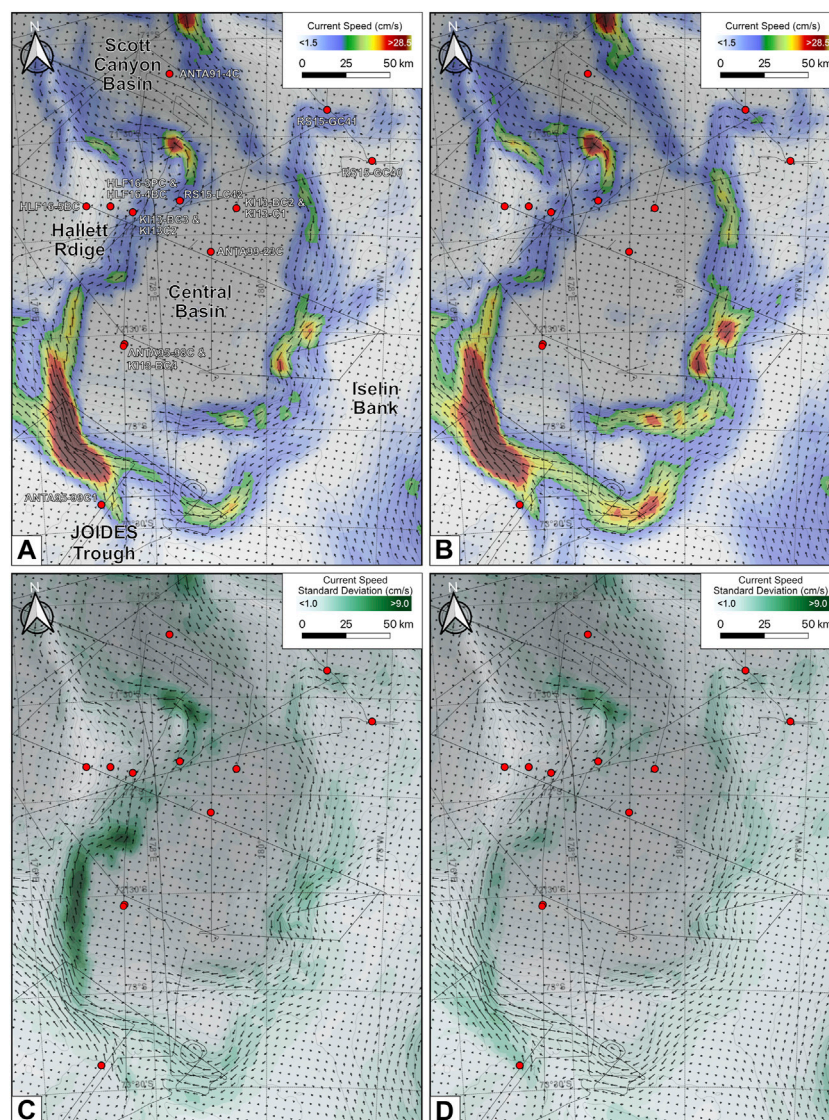


**FIGURE 10**

(A) Average austral winter bottom current speed and direction (1999–2013) obtained from the ocean circulation model. Arrows represent direction, and colors indicate velocity magnitude. Red dots indicate sediment core locations. (B) Average austral summer bottom current speed and direction (2000–2014). (C) Standard deviation of bottom current speed during austral winter (1999–2013). (D) Standard deviation of bottom current speed during austral summer (1999–2014).

above RSU2, deviating from the trend observed in the underlying units between RSU4 to RSU2.

## 5.2 Acoustic facies in the SBP data

The acoustically stratified character of Facies S in the SBP data can be attributed to the presence of alternating intervals characterized by higher acoustic impedance, consisting of coarse-grained material, and intervals with lower acoustic impedance, comprising fine-grained sediment (Neto et al., 2013). The coarse-grained intervals within Facies S are likely the result of iceberg rafting (Joe et al., 2020) and/or winnowing by bottom currents (Kim et al., 2020) commonly found in glaciated continental margins. In contrast, the fine-grained intervals are likely formed by hemipelagic

settling (hemipelagic drape), turbid meltwater plumes (post-glacial mud), or sedimentation influenced by bottom currents (contourites), as documented in previously studies conducted in glaciated continental margins (Anderson et al., 1979; Taylor et al., 2002; Ó Cofaigh et al., 2003; Matthiessen et al., 2010; Lucchi et al., 2013). These depositional processes have been occurred on the lower slope and in the northern part of the Central Basin for an extended period, spanning multiple glacial-interglacial cycles over at least the past 1.34 million years, as inferred from the analysis of core RS15-LC42 (Bollen et al., 2022).

As described in Section 3.1, Facies S can be subdivided into two subtypes based on its resolvable thickness in the SBP data. The presence of large thicknesses of Facies Sh and moderate to low backscatter intensities from MBES data suggests the deposition of less compacted sediment and hence a smaller acoustic impedance contrast at the seabed, allowing

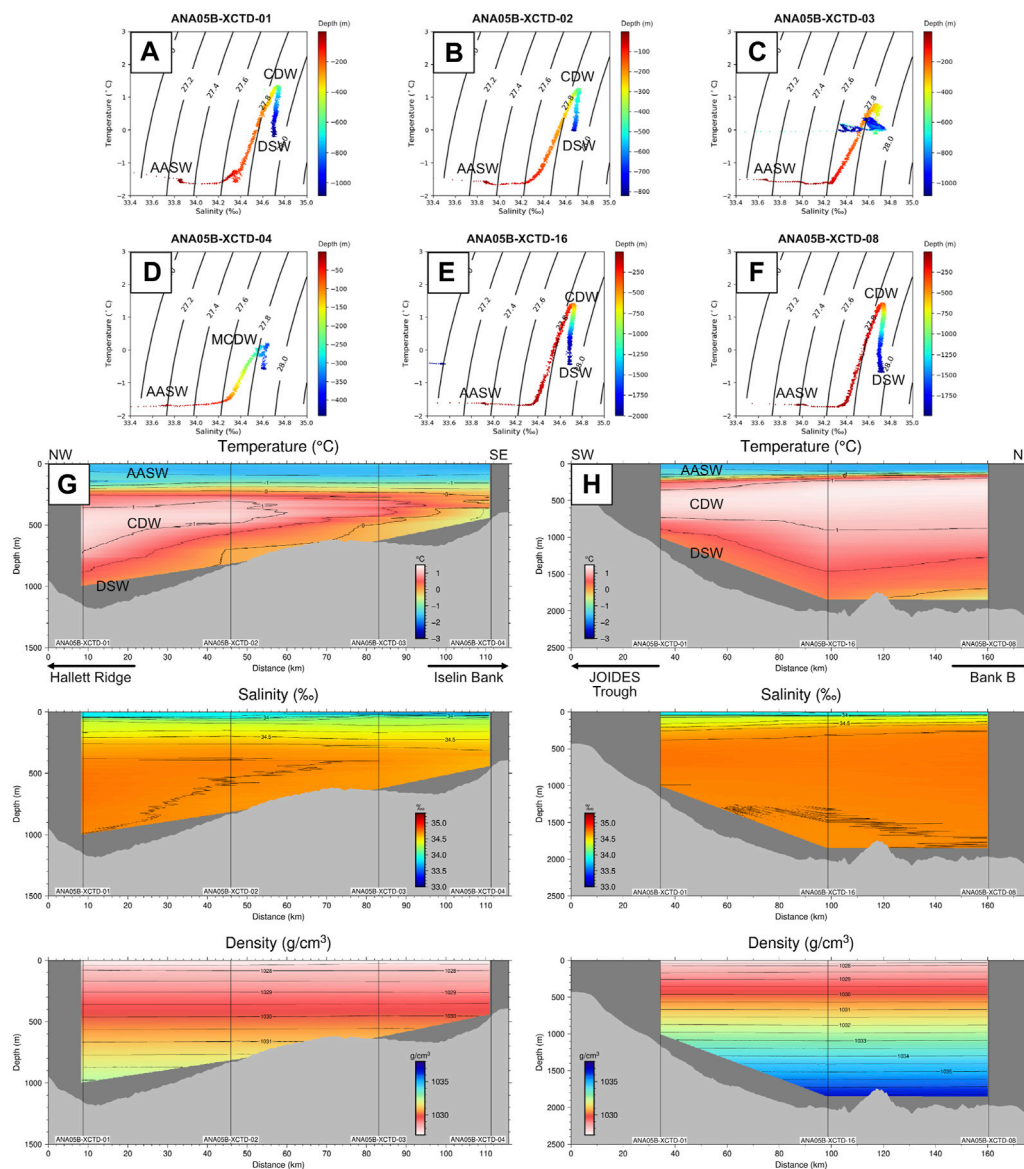
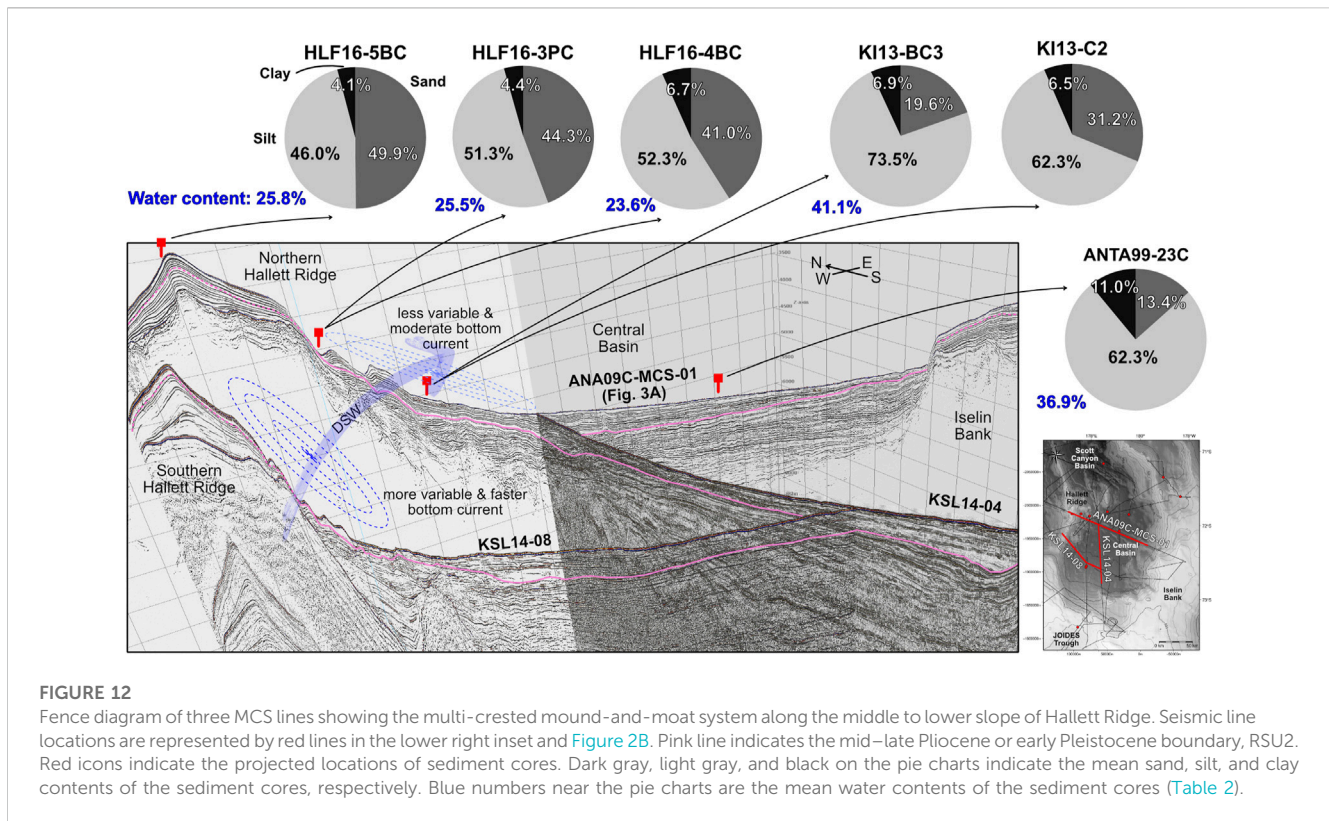


**FIGURE 11**

(A–F) Expandable conductivity-temperature-depth (XCTD) profiles acquired in February 2015 illustrating the cascading of DSW into the Central Basin along the eastern slope of Hallett Ridge. XCTD locations are represented by blue squares in Figure 2B. (G) Temperature-salinity-density structures obliquely crossing from the mid-slope to the outer shelf beyond the JOIDES Trough mouth using the ANA05B-XCTD-01 to 04 (A–D). (H) Temperature-salinity-density structures from the outer shelf of the JOIDES Trough to Bank B in the northern Central Basin using the ANA05B-XCTD-01, –16, and –08 (A,E,F).

deeper penetration (e.g., Fransner et al., 2018; Huang et al., 2018). This interpretation is supported by the sediment cores recovered from Facies Sh, which exhibit relatively low average sand contents with high water contents (KI13-BC3, KI13-C2, RS15-LC42, and ANTA99-23C in Figures 9, 12; Table 1). In contrast to Facies Sh, the weakly stratified nature of Facies Sw is relatively thin (<10 m), suggesting a shallower penetration into the seafloor. We attribute this observation to the presence of a denser and/or coarser sediment layer within Facies Sw. Supporting this interpretation, we note the high backscatter intensity observed in the seafloor's MBES data, as well as the high sand contents and low water contents found in cores HLF16-3PC, HLF16-4BC, and HLF16-5BC (Figures 9, 12).

The absence of internal structure, coupled with the irregular external geometry and truncation of underlying strata exhibited by Facies T can be related with rapid deposition, internal deformation, and basal erosion (Veeken and van Moerkerken, 2013). In the glaciated continental margins, these characteristics of Facies T are consistent with the presence of subglacial tills on the continental shelf (Ó Cofaigh et al., 2005; Dove et al., 2014; Halberstadt et al., 2016; Bart et al., 2017; Kim et al., 2021), as well as mass transport deposits formed by submarine slides, slumps, or glaciogenic debris flows on slopes (Vorren and Laberg, 1997; Ó Cofaigh et al., 2003; Donda et al., 2008; Joe et al., 2020; Kim et al., 2021). The gravity-driven downslope sedimentary processes that form these massive



deposits are significantly influenced by the advance and retreat of grounded ice masses.

### 5.3 Surficial sedimentary and geomorphic features

The surficial sediments on the elongated contourite mound along the Hallett Ridge (Figures 3B, 5B) exhibit distinctive characteristics, including the presence of Facies Sw (Figure 4A), high backscatter intensity (Figures 5B, 6B), and high sand contents (Figures 9, 12; Table 1). Furthermore, the significantly high sand content (65.2%) observed in core RS15-GC40, obtained from shallow depth of the northern part of the Iselin Bank, in conjunction with the formation of a thinly developed sedimentary layer, provides support for the hypothesis that the bathymetric highs surrounding the Central Basin were subjected to winnowing effects caused by the fast-flowing along-slope bottom currents. However, the modeled present-day current speed in this region indicates relatively low, with values below 5 cm/s (Figures 10A, B) and low variabilities (Figures 10C, D). This suggests that the present-day open marine or ice distal oceanographic condition differs from the past ice marginal or glaciomarine environments which experienced significant influence from vigorous bottom current-induced winnowing of fine-grained sediments (e.g., Conte et al., 2021). One potential explanation for the high sand content observed on the crest of Hallett Ridge is that the preferential deposition of fine-grained sediments on the lower slope, rather than on the shallow ridge crest, can be attributed to the downslope sediment-gravity flows (such as debris flows and turbidity currents)

and meltwater discharge from the advanced ice sheet during the past glacial periods. This may occur due to the presence of the bathymetric high, which acts as a barrier and restricts the flow of relatively dense sediment-laden bottom currents over the Hallett Ridge. Consequently, the crest of the Hallett Ridge exhibits a relatively high sand content due to the scarcity of fine-grained sediments in comparison to the lower slope, where a significant accumulation of fine-grained sediment occurs in a low-energy deep-sea depositional environment. Another possibility is that winnowing may have occurred, supported by the intensified along-slope bottom currents (i.e., ASC in Figure 1) during the windier glacial period (Thompson et al., 2018; Kim et al., 2020). The wind-driven ASC likely played a significant role in these winnowing processes. Furthermore, in conjunction with the advancement of ice sheets during that time, there would have been an increased supply of coarser fractions (e.g., McKay et al., 2019; Conte et al., 2021; Gales et al., 2023). These combined processes likely contributed to the current low proportion of fine-grained sediments and the thin unconsolidated deposits found in the upper sections of Hallett Ridge and Iselin Bank.

The contrasting thickness of Facies S on the multi-crested mound and moat system on the northeastern and southeastern part of Hallett ridge indicate that the accumulation of fine-grained sediment is highly affected by bottom currents (McCave and Swift, 1976; McCave and Hall, 2006) in the northern part than southern part. The spatial distribution of Facies Sh (Figure 4A) generally corresponds to regions characterized by moderately-flowing bottom currents (~8–15 cm/s) along the lower slope of the northern Hallett Ridge and Bank B (Figures 4A, 10A, B). These bottom currents possess the capacity to entrain, transport, and selectively release fine-grained

sediments on the seafloor, aligning with the bedform-velocity matrix for deep-water bottom-current systems (Rebesco et al., 2014). These environmental conditions create favorable circumstances for the accumulation of fine-grained sediment, as evident in the recorded characteristics of Facies Sh. Whereas, the southeastern flank of the Hallett Ridge, characterized by Facies Sw and higher backscatter intensity, is influenced by the northward flowing fast bottom current (>15 cm/s) with higher fluctuation as shown in the ROMS model (Figure 10). Based on the findings from geophysical, sedimentological, and oceanographic analyses, it can be inferred that Facies Sh originated within a moderate to low energy conditions. This environment is situated in a deep-water slope setting. This trend is consistent with long-term development of multi-crested mounds depicted in the MCS data (Figure 12). In addition, the amplitude of undulation also increased northward, indicating that the active sedimentation of the mound increases the relief from the moat to the crest of the mound.

The presence of isolated sediment bodies characterized as Facies T in the northwestern region of the Central Basin (Figures 3D, 4B) can be interpreted as mass transport deposit resulting from slope failures. The absence of internal structure, erosional basal boundary, and irregular-shaped external geometry observed in both MCS and SBP data indicate this mass transport deposit were formed by short-lived sedimentary processes. This interpretation can be supported by the identification of side scarps associated with slope failures in the MBES bathymetric data (Figure 6A), as well as similar seismic and geomorphic characteristics of mass transport deposits from previous studies conducted in the eastern Ross Sea margin and Arctic Ocean (e.g., Conte et al., 2021; Schlager et al., 2021; Gales et al., 2023). Westward thickening of the seismostratigraphic unit above RSU2 in the MCS profile (Figure 3A) is partly attributed by this mass transport deposit on the lower slope of Hallett Ridge.

The estimated volume of the mass transport deposit, derived from sparse seismic grids, is  $\sim 9.7 \text{ km}^3$ . This volume falls within the simply calculated range of  $\sim 8.8\text{--}11 \text{ km}^3$ , which is determined based on the area of the trapezoid-shaped depression ( $\sim 220 \text{ km}^2$ ) and the relief of the side scarps ( $\sim 40\text{--}50 \text{ m}$ ) (Figures 3D, 4D, 6). Based on this observation, we can infer that the mass transport deposit originated from the failure of the slope of the well-developed multi-crested mound. In addition, moderate to low backscatter intensity in the area of the trapezoid-shaped depression (Figure 6B) consistent with occurrence of Facies Sh (Figure 4D), indicate that fine-grained sediment accumulation within the depression was continued after the major slope failure occurred. The presence of wrinkled or hummocky seafloor features with moderate backscatter intensity observed in proximity to the side scarps (right inset of Figure 6B) can be considered to be indicative of sedimentary blocks generated by mass transport processes. Furthermore, similar seafloor features, such as a group of small conical mounds around the steep slopes of Bank A, Bank B, and the western slope of Iselin Bank (Figures 7, 8), are also likely associated with mass wasting by smaller scale slope failures. These rough seafloor features and inhomogeneous subsurface sedimentary deposits tend to increase the backscatter intensity (Jackson et al., 1986; Mitchell, 1993).

The widespread Facies T deposits near the JOIDES Trough mouth (Figure 4B) suggests their origin from subglacial or ice-marginal sedimentation during the advancement of the grounded ice sheet near the paleo-shelf break (Ó Cofaigh et al., 2003; e.g.;

Batchelor and Dowdeswell, 2014). These deposits exhibit distinct characteristics compared to the slope failure deposits found on the lower slope of northeastern Hallett Ridge. On the lower slope and the southern Central Basin floor, stacked debris flow deposits with moderated backscatter intensity can be observed (Figures 4C, 5B, 8A, B). However, the stacked debris flow deposits observed on the upper slope and the grounding zone wedge on the outer shelf show higher backscatter intensity (Figures 4B, E, 9), which can be attributed to the roughness of seafloor and inhomogeneities of subsurface sediments (Jackson et al., 1986; Mitchell, 1993). According to the ROMS model (Figures 10A, B), we identified vigorous, fast-flowing bottom currents (>20 cm/s) traversing the outer shelf and upper slope beyond the JOIDES Trough mouth and the southeastern flank of the Hallett Ridge. These areas with elevated current speeds correspond to the regions displaying Facies T (Figure 4B) and relatively high MBES backscatter intensity (Figure 9). The unusually short penetration depth observed in the nearest gravity core ANTA95-99C1 ( $\sim 71 \text{ cm}$ , Table 2; Figure 9) suggests the presence of relatively coarser sediments that hinders deep sampling. Based on these results, we infer the glaciogenic sedimentary deposits on the outer shelf and upper slope beyond the JOIDES Trough mouth as mainly composed of coarse-grained sediment, contrasting with the stacked debris flow deposits on the lower slope. These deposits are largely influenced by the winnowing process induced by fast-flowing bottom currents, which hinders the accumulation of fine-grained particles within the surface sediment layer (Stow, 2002; Conte et al., 2021; Bollen et al., 2022).

The elongated stripes of low backscatter intensities, observed near the undulations of the southern Hallett Ridge (Figure 5B), coincide with the presence of  $\sim 15\text{--}17 \text{ m}$  thick deposits of Facies Sh, which are separated by a sediment-starved trough (Figure 4C). These features, characterized by their northward elongation as observed in the 7.5 km-width MBES bathymetry and backscatter grids, along with well-developed sediment accumulation on both sides of the trough, suggest the presence of a submarine channel-levee system (e.g., Fransner et al., 2018; Boggild and Mosher, 2021). Unlike larger-scale, deeply incised submarine canyons such as the Hillary Canyon and Bowers Canyon beyond the Pennell Trough and Drygalski Trough, this submarine channel exhibits smaller dimensions and lacks distinct side scarps. This indicates that the gravity flows responsible for forming the submarine channel in the JOIDES Trough and Central Basin region were less erosive than those occurring in the Hillary and Bowers Canyons. The westward-deflected outflow of DSW along the eastern flank of Hallett Ridge, influenced by the Coriolis effect, may encounter reduced overall speeds due to the semi-closed geometry of the Central Basin, attributed to bathymetric obstacles and narrow gateways (Figures 10A, B). This is evident from the confined path of DSW spreading widely in the northern part of the basin as shown in a recently published modeling result, which demonstrated the presence of dense shelf water exceeding 200 m in thickness in the Central Basin (Morrison et al., 2020) (Figure 2A). The existence of Bank B and the narrow gateway of the NE Gap (Figure 2A), serves as an effective obstruction that blocks the northward flow of DSW from the northern Central Basin toward the Scott Canyon Basin. These bathymetric barriers functions in a manner similar to a low dam or weir, impeding the northward movement of water. As a result, the denser water accumulated in the northern part of the Central Basin

can be reaccelerated at the NE Gap due to the steep gradient, leading to the erosion of underlying strata and the subsequent formation of the Scott Canyon, characterized by its deeply incised nature. The distinctive bathymetric features of the Central Basin provide an explanation for the presence of smaller-scale channel-levee systems on the lower slope beyond the JOIDES Trough, as well as the initiation of the Scott Canyon in deeper environments.

## 5.4 Influence of ice sheet dynamics and ocean circulation on contourite development

Previous studies have documented multiple advances of a grounded ice sheet in the vicinity of the JOIDES Trough near the continental shelf edge during Quaternary glacial cycles (Brancolini et al., 1995; Bart et al., 2011; Kim et al., 2018; Bollen et al., 2022). Based on the seismostratigraphic interpretation in the Central Basin (Kim et al., 2018), the contourites developed simultaneously with the formation of the topset-truncated trough-mouth fan beyond the mouth of the JOIDES Trough since the time of RSU2 (the mid-late Pliocene or early Pleistocene). The sediments deposited beyond the shelf edge by grounded ice during glacial maxima were influenced by down-slope debris and turbidity flows during deglacial and interglacial periods, together with the sediment-starved submarine channel thalweg and the formation of levee systems in the southwestern Central Basin (Figures 4C, 12). We propose that the suspended fine-grained components of such flows, remobilized by bottom currents, have contributed to the formation of contourites on the crest and flanks of Hallett Ridge after the time of formation of RSU2. RSU2 marks the major transition to the modern cold dry-based Antarctic ice sheet (Rebesco et al., 2006; McKay et al., 2012), and the observed northward thickening of the multi-crested mounds in the MCS data (above RSU2, Figures 3A, 12) can be explained by an advanced grounding line further north. This interpretation aligns with previous studies suggesting active sedimentation controlled by bottom currents on the middle to lower slope of northern Hallett Ridge (Khim et al., 2021; Torricella et al., 2021; Bollen et al., 2022).

As the interpretation of Facies S in Section 5.2, the subparallel internal reflections observed in the stratified sedimentary deposits are indicative of changes in the sedimentary processes, which may be attributed to variations in bottom current strength, potentially influenced by processes such as DSW export during glacial and interglacial periods. As the grounded ice sheet approached the shelf break, it is likely that DSW cascading diminished or ceased due to the absence of factors that promote the production of dense water, such as large ice shelves, coastal polynyas, and large cross-shelf depressions (Amblas and Dowdeswell, 2018; Bollen et al., 2022). In contrast, DSW export was most vigorous during interglacial periods (Bollen et al., 2022; Kim et al., 2023), creating an oceanographic setting conducive to the formation of contourites (Thran et al., 2018). During the LGM, the grounding line of the ice sheet at the JOIDES Trough mouth is believed to have been located more than 100 km landward of the shelf break (Anderson et al., 2014; Halberstadt et al., 2016; Prothro et al., 2020). A recent investigation of sediment core RS15-LC42 has suggested that partial advances of grounded ice in the JOIDES Trough may have occurred during “mild” glacial periods within the past

0.3 Myr and during 1.4–1.2 Ma (Bollen et al., 2022). In addition, the partial advances of the grounded ice can explain the lack of the deep incisions (e.g., submarine canyon and gullies) on the gentle upper slope beyond the JOIDES Trough mouth similar to the Pennell Trough mouth in the eastern Ross Sea (e.g., Gales et al., 2021). If the well-developed contourites along the Hallett Ridge above RSU2 primarily formed due to active bottom-current processes intensified by DSW export, it can be inferred that DSW export sustained by the partial advance of the ice sheet during mild glaciations and the over-deepened morphology of the outer shelf (Figure 2A) significantly contributed to the development of the contourites. Pleo-circulation modelling and deep drilling is needed to verify this hypothesis.

The occurrence of slope failures on the eastern flank of northern Hallett Ridge can be attributed to the high accumulation of sediment caused by the advancement of the grounded ice sheet near the shelf break, as indicated by previous studies (e.g., Lucchi et al., 2002; McKay et al., 2019; Conte et al., 2021). The preferential deposition of fine-grained sediments on the northern Hallett Ridge, due to the slowed northward-flowing DSW caused by the semi-closed geometry of the Central Basin, may have resulted in an elevation of pore pressure within the weak, water-rich interglacial sediments interbedded with low permeable glaciogenic sediments (e.g., Gales et al., 2023). This increase in pore pressure likely contributes to slope instability and serves as a causal factor for the observed slope failures (e.g., Long et al., 2003; Laberg and Camerlenghi, 2008; Miramontes et al., 2018). Glacio-isostatic rebound associated with the retreat of the grounded ice sheet could have triggered slope failure in inherently vulnerable contourite deposits (Kaufmann et al., 2005; Whitehouse et al., 2019; Gales et al., 2023), as observed in the northwestern part of the Central Basin.

## 6 Conclusion

The mutually reinforcing evidence of the geophysical, sedimentological, and oceanographic analyses presented in this study lead to a reliable inference of past and modern sedimentary and geomorphic processes in the northwestern Ross Sea margin. The combined results indicate that the westward-deflected DSW cascading in the northwestern Ross Sea margin likely contributed to the formation of the well-developed contourite deposits lying on and along the Hallett Ridge. The northward thickening of multi-crested mounds above RSU2 and of the stratified surficial sediments of Facies S reflects a progressive northward shift of the sediment source from the advanced grounded ice sheet since Late Pliocene global cooling. Active bottom-current processes enhanced by DSW export during interglacial periods and mild glaciations with partial advance of the grounded ice sheet may have contributed substantially to the development of contourites on and along Hallett Ridge. The preferential accumulation of fine-grained sediments on northern Hallett Ridge as a result of slowed DSW due to the semi-closed basin geometry may have increased slope instability and caused slope failures. This study demonstrates the high potential for multidisciplinary studies to find geological archives that are critical to ice sheet and circulation reconstructions.

## Data availability statement

The datasets presented in this study can be found in online repositories. The names of the repository/repositories and accession number(s) can be found below: <https://kpsc.kopri.re.kr> Korea Polar Data Center.

## Author contributions

SoK and LD conceptualized and designed the study. SoK wrote the first draft of the manuscript and performed significant editing and revisions with input from all co-authors. JH, S-GK, HK, YC, HC, and YP were involved in geophysical data acquisition, processing, and interpretation. EC, SuK, ML, AG, JL, and K-CY contributed to obtaining sediment cores samples and conducted sedimentological analysis and interpretation. AB conducted ocean bottom current modeling and oceanographic interpretation. S-HL assisted in data interpretation and result discussion. All authors contributed to the article and approved the submitted version.

## Funding

This work was supported by grants from the Korea Polar Research Institute funded by the Ministry of Oceans and Fisheries (PE23050 and PE23090). This work was partly funded by the Korea-Italy Bilateral Program (2019K1A3A1A25000116) by National Research Foundation of Korea and by the Italian National Antarctic Research Program (PNRA)–ROSSLOPE Project (2010/A2.07) and partly co-funded by the Italian Foreign Ministry

## References

- Amblas, D., and Dowdeswell, J. A. (2018). Physiographic influences on dense shelf-water cascading down the Antarctic continental slope. *Earth-Science Rev.* 185, 887–900. doi:10.1016/j.earscirev.2018.07.014
- Anderson, J. B., and Bartek, L. R. (1992). "Cenozoic glacial history of the Ross Sea revealed by intermediate resolution seismic reflection data combined with drill site information," in Contributions to antarctic research III *antarctic research series*. Editor D. H. Elliot (Washington, D.C., United States: American Geophysical Union), 231–263.
- Anderson, J. B., Conway, H., Bart, P. J., Witus, A. E., Greenwood, S. L., McKay, R. M., et al. (2014). Ross Sea paleo-ice sheet drainage and deglacial history during and since the LGM. *Quat. Sci. Rev.* 100, 31–54. doi:10.1016/j.quascirev.2013.08.020
- Anderson, J. B., Kurtz, D., and Weaver, F. M. (1979). "Sedimentation on the Antarctic continental slope," in Geology of continental slopes *special publication*. Editors L. J. Doyle and O. Pilkey (Tulsa: SEPM), 265–283.
- Armitage, T. W. K., Kwok, R., Thompson, A. F., and Cunningham, G. (2018). Dynamic topography and sea level anomalies of the Southern Ocean: variability and teleconnections. *J. Geophys. Res. Oceans* 123, 613–630. doi:10.1002/2017JC013534
- Bart, P., Anderson, J., Trincardi, F., and Shipp, S. (2000). Seismic data from the northern basin, Ross Sea, record extreme expansions of the East antarctic ice sheet during the late neogene. *Mar. Geol.* 166, 31–50. doi:10.1016/s0025-3227(00)00006-2
- Bart, P. J., Anderson, J. B., and Nitsche, F. (2017). Post-LGM grounding-line positions of the bindschadler paleo ice stream in the Ross Sea embayment, Antarctica. *J. Geophys. Res. Earth Surf.* 122, 1827–1844. doi:10.1002/2017jf004259
- Bart, P. J., and De Santis, L. (2012). Glacial intensification during the neogene: a review of seismic stratigraphic evidence from the Ross Sea, Antarctica, continental shelf. *Oceanography* 25, 166–183. doi:10.5670/oceanog.2012.92
- Bart, P. J., Sjunneskog, C., and Chow, J. M. (2011). Piston-core based biostratigraphic constraints on Pleistocene oscillations of the West antarctic ice sheet in western Ross Sea between north Basin and AND-1B drill site. *Mar. Geol.* 289, 86–99. doi:10.1016/j.margeo.2011.09.005
- (MAECI)–STREAM Project. SoK and S-HL were funded by the Korea Institute of Energy Technology Evaluation and Planning (KETEP) and the Ministry of Trade, Industry, and Energy (MOTIE) of the Republic of Korea (No. 20212010200020).
- Batchelor, C. L., and Dowdeswell, J. A. (2014). The physiography of High Arctic cross-shelf troughs. *Quat. Sci. Rev.* 92, 68–96. doi:10.1016/j.quascirev.2013.05.025
- Bergamasco, A., Defendi, V., Zambianchi, E., and Spezie, G. (2002). Evidence of dense water overflow on the Ross Sea shelf-break. *Antarct. Sci.* 14, 271–277. doi:10.1017/s0954102002000068
- Bjordal-Olsen, S., Rydningen, T. A., Laberg, J. S., Lasabuda, A. P. E., and Knutsen, S.-M. (2023). Contrasting neogene–quaternary continental margin evolution offshore mid-north Norway: implications for source-to-sink systems. *Mar. Geol.* 456, 106974. doi:10.1016/j.margeo.2022.106974
- Blott, S. J., and Pye, K. (2001). GRADISTAT: a grain size distribution and statistics package for the analysis of unconsolidated sediments. *Earth Surf. Process. Landforms* 26, 1237–1248. doi:10.1002/esp.261
- Boggild, K., and Mosher, D. C. (2021). Turbidity currents at polar latitudes: a case study of NP-28 channel in the amundsen basin, Arctic Ocean. *Mar. Geol.* 440, 106571. doi:10.1016/j.margeo.2021.106571
- Bollen, M., Riesselman, C. R., Ohneiser, C., Albot, O., McKay, R., Lee, M. K., et al. (2022). Pleistocene oceanographic variability in the Ross Sea: a multiproxy approach to age model development and paleoenvironmental analyses. *Glob. Planet. Change* 216, 103901. doi:10.1016/j.gloplacha.2022.103901
- Brancolini, G., Cooper, A. K., and Coren, F. (1995). "Seismic facies and glacial history in the western Ross Sea (Antarctica)," in Geology and seismic Stratigraphy of the antarctic margin *antarctic research series*. Editors A. K. Cooper, P. F. Barker, and G. Brancolini (United States: Wiley Online Library), 209–233.
- Budillon, G., Castagno, P., Aliani, S., Spezie, G., and Padman, L. (2011). Thermohaline variability and Antarctic bottom water formation at the Ross Sea shelf break. *Deep Sea Res. Part I Oceanogr. Res. Pap.* 58, 1002–1018. doi:10.1016/j.dsr.2011.07.002
- Budillon, G., Cordero, S. G., and Salusti, E. (2002). On the dense water spreading off the Ross Sea shelf (Southern Ocean). *J. Mar. Syst.* 35, 207–227. doi:10.1016/S0924-7963(02)00082-9

## Acknowledgments

The authors express their deep appreciation to the captain and crew of the R/V *Araon* for their invaluable assistance during the Antarctic expeditions. Additionally, the authors are grateful to Prof. R. M. McKay from Victoria University of Wellington for generously providing the grain-size results for RS15-LC42. We thank the editor and two reviewers for their constructive comments that improved the manuscript.

## Conflict of interest

The authors declare that the research was conducted in the absence of any commercial or financial relationships that could be construed as a potential conflict of interest.

## Publisher's note

All claims expressed in this article are solely those of the authors and do not necessarily represent those of their affiliated organizations, or those of the publisher, the editors and the reviewers. Any product that may be evaluated in this article, or claim that may be made by its manufacturer, is not guaranteed or endorsed by the publisher.

- Cande, S. C., and Stock, J. M. (2004). "Constraints on late cretaceous and cenozoic extension in the Ross Sea from the southwest pacific plate circuit," in *Eos transactions American geophysical union* (New Jersey, United States: Wiley).
- Cande, S. C., Stock, J. M., Müller, R. D., and Ishihara, T. (2000). Cenozoic motion between east and west Antarctica. *Nature* 404, 145–150. doi:10.1038/35004501
- Carter, L., Bostock-Lyman, H., and Bowen, M. (2022). "Chapter 4 - water masses, circulation and change in the modern Southern Ocean," in *Antarctic climate evolution*. Editors F. Florindo, M. Siebert, L. D. Santis, and T. Naish (Amsterdam: Elsevier), 165–197. doi:10.1016/B978-0-12-819109-5.00003-7
- Chavanne, C. P., Heywood, K. J., Nicholls, K. W., and Fer, I. (2010). Observations of the antarctic slope undercurrent in the southeastern weddell sea. *Geophys. Res. Lett.* 37. doi:10.1029/2010GL043603
- Conte, R., Rebesco, M., Santis, L. D., Colleoni, F., Bensi, M., Kovacevic, V., et al. (2021). Bottom current control on sediment deposition between the Iselin Bank and the hillary canyon (Antarctica) since the late Miocene: an integrated seismic-oceanographic approach. *Deep-Sea Res. Part I* 176, 103606. doi:10.1016/j.dsr.2021.103606
- Cunningham, S. A., Alderson, S. G., King, B. A., and Brandon, M. A. (2003). Transport and variability of the antarctic circumpolar current in drake passage. *J. Geophys. Res. Oceans* 108, 1978–2012. doi:10.1029/2001JC001147
- Davey, F., and Brancolini, G. (1995). "The late mesozoic and cenozoic structural setting of the Ross Sea region," in *Geology and seismic Stratigraphy of the antarctic margin antarctic research series*. Editors A. K. Cooper, P. F. Barker, and G. Brancolini (Washington, D.C., United States: American Geophysical Union), 167–182.
- Davey, F. J., Cande, S., and Stock, J. (2021). Cenozoic continental rifting in the north-western Ross Sea. *null* 65, 389–396. doi:10.1080/00288306.2021.1891942
- Davey, F. J. (2004). *Ross Sea bathymetry*. Lower Hutt, New Zealand: Institute of Geological and Nuclear Science Limited.
- De Santis, L., Anderson, J. B., Brancolini, G., and Zayatz, I. (1995). "Seismic record of late Oligocene through Miocene glaciation on the central and eastern continental shelf of the Ross Sea," in *Geology and seismic Stratigraphy of the antarctic margin antarctic research series*. Editors A. K. Cooper, P. F. Barker, and G. Brancolini (Washington, D.C., United States: American Geophysical Union), 235–260.
- De Santis, L., Prato, S., Brancolini, G., Lovo, M., and Torelli, L. (1999). The eastern Ross Sea continental shelf during the cenozoic: implications for the West antarctic ice sheet development. *Glob. Planet. Change* 23, 173–196. doi:10.1016/S0921-8181(99)00056-9
- Donda, F., O'Brien, P., De Santis, L., Rebesco, M., and Brancolini, G. (2008). Mass wasting processes in the western wilkes land margin: possible implications for East Antarctic glacial history. *Palaeogeogr. Palaeoclimatol. Palaeoecol.* 260, 77–91. doi:10.1016/j.palaeo.2007.08.008
- Dorschel, B., Hehemann, L., Viquerat, S., Warnke, F., Dretter, S., Tenberge, Y. S., et al. (2022). The international bathymetric chart of the Southern Ocean Version 2. *Sci. Data* 9, 275. doi:10.1038/s41597-022-01366-7
- Dove, D., Polyak, L., and Coakley, B. J. (2014). Widespread, multi-source glacial erosion on the Chukchi margin, Arctic Ocean. *Quat. Sci. Rev.* 92, 112–122. doi:10.1016/j.quascirev.2013.07.016
- Dowdeswell, J. A., Evans, J., Ó Cofaigh, C., and Anderson, J. B. (2006). Morphology and sedimentary processes on the continental slope off pine island bay, amundsen sea, west Antarctica. *GSA Bull.* 118, 606–619. doi:10.1130/B25791.1
- Fransner, O., Noormets, R., Flink, A. E., Hogan, K. A., and Dowdeswell, J. A. (2018). Sedimentary processes on the continental slope off Kvitøya and Albertini troughs north of Nordaustlandet, Svalbard – the importance of structural-geological setting in trough-mouth fan development. *Mar. Geol.* 402, 194–208. doi:10.1016/j.margeo.2017.10.008
- Friedman, G. M., and Sanders, J. E. (1978). *Principles of sedimentology*. New Jersey, United States: John Wiley and Sons.
- Gales, J. A., McKay, R. M., De Santis, L., Rebesco, M., Laberg, J. S., Shevenell, A. E., et al. (2023). Climate-controlled submarine landslides on the Antarctic continental margin. *Nat. Commun.* 14, 2714. doi:10.1038/s41467-023-38240-y
- Gales, J. A., Rebesco, M., De Santis, L., Bergamasco, A., Colleoni, F., Kim, S., et al. (2021). Role of dense shelf water in the development of Antarctic submarine canyon morphology. *Geomorphology* 372, 107453. doi:10.1016/j.geomorph.2020.107453
- García, M., Hernández-Molina, F. J., Alonso, B., Vázquez, J. T., Ercilla, G., Llave, E., et al. (2016). Erosive sub-circular depressions on the Guadalquivir bank (gulf of cadiz): interaction between bottom current, mass-wasting and tectonic processes. *Mar. Geol.* 378, 5–19. doi:10.1016/j.margeo.2015.10.004
- Gordon, A. L., Huber, B. A., and Buseck, J. (2015). Bottom water export from the western Ross Sea, 2007 through 2010. *Geophys. Res. Lett.* 42, 5387–5394. doi:10.1002/2015gl064457
- Gordon, A. L., Orsi, A. H., Muench, R., Huber, B. A., Zambianchi, E., and Visbeck, M. (2009). Western Ross Sea continental slope gravity currents. *Deep Sea Res. Part II Top. Stud. Oceanogr.* 56, 796–817. doi:10.1016/j.dsr2.2008.10.037
- Granot, R., Cande, S., Stock, J., Davey, F., and Clayton, R. (2010). Postspreading rifting in the Adare Basin, Antarctica: regional tectonic consequences. *Geochem. Geophys. Geosystems* 11. doi:10.1029/2010gc003105
- Halberstadt, A. R. W., Simkins, L. M., Greenwood, S. L., and Anderson, J. B. (2016). Past ice-sheet behaviour: retreat scenarios and changing controls in the Ross Sea, Antarctica. *Cryosphere* 10, 1003–1020. doi:10.5194/tc-10-1003-2016
- Harris, P. T., Macmillan-Lawler, M., Rupp, J., and Baker, E. K. (2014). Geomorphology of the oceans. *Mar. Geol.* 352, 4–24. doi:10.1016/j.margeo.2014.01.011
- Hochmuth, K., Gohl, K., Leitchenkov, G., Sauerlich, I., Whittaker, J. M., Unzelmann-Neben, G., et al. (2020). The evolving paleobathymetry of the circum-antarctic Southern Ocean since 34 Ma – A key to understanding past cryosphere-ocean developments. *Geochem. Geophys. Geosystems* 21, e2020GC009122. doi:10.1029/2020GC009122
- Howe, J. A., Stoker, M. S., Stow, D. A. V., and Akhurst, M. C. (2002). "Sediment drifts and contourite sedimentation in the northeastern rockall Trough and faroe-shetland channel, north atlantic ocean," in *Deep-water contourite systems: modern drifts and ancient rivers, seismic and sedimentary characteristics geological society, London, memoirs*. Editors D. A. V. Stow, C. J. Pudsey, J. A. Howe, J.-C. Faugetes, and A. R. Viana (United Kingdom: The Geological Society of London), 65–72.
- Huang, X., Gohl, K., and Jokat, W. (2014). Variability in Cenozoic sedimentation and paleo-water depths of the Weddell Sea basin related to pre-glacial and glacial conditions of Antarctica. *Glob. Planet. Change* 118, 25–41. doi:10.1016/j.gloplacha.2014.03.010
- Huang, Z., Siwabessy, J., Cheng, H., and Nichol, S. (2018). Using multibeam backscatter data to investigate sediment-acoustic relationships. *J. Geophys. Res. Oceans* 123, 4649–4665. doi:10.1029/2017JC013638
- Jackson, D. R., Winebrenner, D. P., and Ishimaru, A. (1986). Application of the composite roughness model to high-frequency bottom backscattering. *J. Acoust. Soc. Am.* 79, 1410–1422. doi:10.1121/1.393669
- Jacobs, S. S., Amos, A. F., and Bruchhausen, P. M. (1970). Ross sea oceanography and antarctic bottom water formation. *Deep Sea Res. Oceanogr. Abstr.* 17, 935–962. doi:10.1016/0011-7471(70)90046-x
- Jacobs, S. S. (2004). Bottom water production and its links with the thermohaline circulation. *Antarct. Sci.* 16, 427–437. doi:10.1017/s095410200400224x
- Jacobs, S. S., Fairbanks, R. G., and Horibe, Y. (1985). "Origin and evolution of water masses near the antarctic continental margin: evidence from H218O/H216O ratios in seawater," in *Oceanology of the antarctic continental shelf* (Washington, D.C., United States: American Geophysical Union), 59–85. doi:10.1029/AR043p0059
- Jacobs, S. S., Giulivi, C. F., and Mele, P. A. (2002). Freshening of the Ross Sea during the late 20th century. *Science* 297, 386–389. doi:10.1126/science.1069574
- Joe, Y. J., Polyak, L., Schreck, M., Niessen, F., Yoon, S. H., Kong, G. S., et al. (2020). Late quaternary depositional and glacial history of the arliss plateau off the East siberian margin in the western Arctic Ocean. *Quat. Sci. Rev.* 228, 106099. doi:10.1016/j.quascirev.2019.106099
- Kaufmann, G., Wu, P., and Ivins, E. R. (2005). Lateral viscosity variations beneath Antarctica and their implications on regional rebound motions and seismotectonics. *J. Geodyn.* 39, 165–181. doi:10.1016/j.jog.2004.08.009
- Kennedy, A. T., Farnsworth, A., Lunt, D. J., Lear, C. H., and Markwick, P. J. (2015). Atmospheric and oceanic impacts of Antarctic glaciation across the Eocene–Oligocene transition. *Philosophical Trans. R. Soc. Lond. A Math. Phys. Eng. Sci.* 373, 20140419. doi:10.1098/rsta.2014.0419
- Kennett, J. P. (1977). Cenozoic evolution of Antarctic glaciation, the circum-Antarctic Ocean, and their impact on global paleoceanography. *J. Geophys. Res.* 82, 3843–3860. doi:10.1029/jc082i027p03843
- Khim, B.-K., Colizza, E., Lee, J. I., Giglio, F., Ha, S., and Bak, Y.-S. (2021). Biological productivity and glaciomarine sedimentation in the Central Basin of the northwestern Ross Sea since the last glacial maximum. *Polar Sci.* 28, 100682. doi:10.1016/j.polar.2021.100682
- Kim, S., Bak, Y.-S., Prebble, J. G., Kang, M.-I., Kim, S., Park, J., et al. (2023). Glacial-interglacial changes in oceanic conditions and depositional process in the continental rise in response to ice sheet (shelf) variation in Bellingshausen Sea, Antarctica. *Front. Mar. Sci.* 10. doi:10.3389/fmars.2023.1183516
- Kim, S., De Santis, L., Hong, J. K., Cottlerle, D., Petronio, L., Colizza, E., et al. (2018). Seismic stratigraphy of the Central Basin in northwestern Ross Sea slope and rise, Antarctica: clues to the late cenozoic ice-sheet dynamics and bottom-current activity. *Mar. Geol.* 395, 363–379. doi:10.1016/j.margeo.2017.10.013
- Kim, S., Lee, J. I., McKay, R. M., Yoo, K.-C., Bak, Y.-S., Lee, M. K., et al. (2020). Late Pleistocene paleoceanographic changes in the Ross Sea - Glacial-interglacial variations in paleoproductivity, nutrient utilization, and deep-water formation. *Quat. Sci. Rev.* 239, 106356. doi:10.1016/j.quascirev.2020.106356
- Kim, S., Polyak, L., Joe, Y. J., Niessen, F., Kim, H. J., Choi, Y., et al. (2021). Seismostratigraphic and geomorphic evidence for the glacial history of the northwestern chukchi margin, Arctic Ocean. *J. Geophys. Res. Earth Surf.* 126, e2020JF006030. doi:10.1029/2020jf006030
- King, M. V., Gales, J. A., Laberg, J. S., McKay, R. M., De Santis, L., Kulhanek, D. K., et al. (2022). Pleistocene depositional environments and links to cryosphere-ocean interactions on the eastern Ross Sea continental slope, Antarctica (IODP Hole U1525A). *Mar. Geol.* 443, 106674. doi:10.1016/j.margeo.2021.106674
- Laberg, J. S., and Camerlenghi, A. (2008). "The significance of contourites for submarine slope stability," in *Contourites developments in sedimentology*. Editors M. Rebesco and A. Camerlenghi (Amsterdam, Netherlands: Elsevier), 537–556. doi:10.1016/S0070-4571(08)10025-5
- Lasabuda, A., Geissler, W. H., Laberg, J. S., Knutsen, S., Rydningen, T. A., and Berglar, K. (2018). Late cenozoic erosion estimates for the northern barents sea: quantifying

- glacial sediment input to the Arctic Ocean. *Geochem. Geophys. Geosystems* 19, 4876–4903. doi:10.1029/2018gc007882
- Lawver, L. A., Gahagan, L. M., and Coffin, M. F. (1992). “The development of paleoseaways around Antarctica,” in *The antarctic palaeoenvironment: a perspective on global change antarctic research series*. Editors J. P. Kennett and D. A. Warnke (Washington, DC): AGU, 7–30.
- Le Heron, D. P., Hogan, K. A., Phillips, E. R., Huuse, M., Busfield, M. E., and Graham, A. G. C. (2019). in *Glaciated margins—the sedimentary and geophysical archive*. Editors D. P. Le Heron, K. A. Hogan, E. R. Phillips, M. Huuse, M. E. Busfield, and A. G. C. Graham (Washington, D.C., United States: Geological Society London).
- Livingstone, S. J., Cofaigh, C., Stokes, C. R., Hillenbrand, C.-D., Vieli, A., and Jamieson, S. S. (2012). Antarctic palaeo-ice streams. *Earth-Science Rev.* 111, 90–128. doi:10.1016/j.earscirev.2011.10.003, Ó
- Long, D., Stevenson, A. G., Wilson, C. K., and Bulat, J. (2003). “Slope failures in the faroe-shetland channel,” in *Submarine mass Movements and their consequences: 1st international symposium advances in natural and technological hazards research series*. Editors J. Locat and J. Mienert (Netherlands: Kluwer Academic Publishers), 281–289.
- López-Quirós, A., Lobo, F. J., Escutia, C., García, M., Hernández-Molina, F. J., Pérez, L. F., et al. (2020). Geomorphology of ana basin, southwestern scotia sea (Antarctica): decoding the spatial variability of bottom-current pathways. *Mar. Geol.* 422, 106113. doi:10.1016/j.margeo.2020.106113
- Lu, H., Fulthorpe, C. S., and Mann, P. (2003). Three-dimensional architecture of shelf-building sediment drifts in the offshore Canterbury Basin, New Zealand. *Mar. Geol.* 193, 19–47. doi:10.1016/S0025-3227(02)00612-6
- Lucchi, R. G., Camerlenghi, A., Rebesco, M., Colmenero-Hidalgo, E., Sierro, F. J., Sagnotti, L., et al. (2013). Postglacial sedimentary processes on the storfjorden and kveithola Trough mouth fans: significance of extreme glacial marine sedimentation. *Glob. Planet. Change* 111, 309–326. doi:10.1016/j.gloplacha.2013.10.008
- Lucchi, R. G., Rebesco, M., Camerlenghi, A., Busetti, M., Tomadin, L., Villa, G., et al. (2002). Mid-late Pleistocene glacial marine sedimentary processes of a high-latitude, deep-sea sediment drift (Antarctic Peninsula Pacific margin). *Mar. Geol.* 189, 343–370. doi:10.1016/S0025-3227(02)00470-X
- Martorelli, E., Petroni, G., Chiocci, F. L., Party, and the, P. S. (2011). Contourites offshore Pantelleria island (sicily channel, mediterranean sea): depositional, erosional and biogenic elements. *Geo-Marine Lett.* 31, 481–493. doi:10.1007/s00367-011-0244-0
- Matthiessen, J., Niessen, F., Stein, R., and Naafs, B. D. A. (2010). Pleistocene glacial marine sedimentary environments at the eastern Mendeleev Ridge, Arctic Ocean. *Polarforschung* 79, 123–137.
- McCave, I. N., and Hall, I. R. (2006). Size sorting in marine muds: processes, pitfalls, and prospects for paleoflow-speed proxies. *Geochem. Geophys. Geosystems* 7. doi:10.1029/2006gc001284
- McCave, I. N., and Swift, S. A. (1976). A physical model for the rate of deposition of fine-grained sediments in the deep sea. *GSA Bull.* 87, 541–546. doi:10.1130/0016-7606(1976)87<541:apmfr>2.0.co;2
- McKay, R. M., Albot, O., Dunbar, G. B., Lee, J. I., Lee, M. K., Yoo, K.-C., et al. (2022). A comparison of methods for identifying and quantifying Ice Rafted Debris on the Antarctic margin. *Paleoceanogr. Paleoclimatology* 37, e2021PA004404. doi:10.1029/2021pa004404
- McKay, R. M., Barrett, P. J., Levy, R. S., Naish, T. R., Gollidge, N. R., and Pyne, A. (2016). Antarctic cenozoic climate history from sedimentary records: aNDRILL and beyond. *Philosophical Trans. R. Soc. Lond. A Math. Phys. Eng. Sci.* 374, 20140301. doi:10.1098/rsta.2014.0301
- McKay, R. M., De Santis, L., and Kulhanek, D. K. (2019). “Expedition 374 scientists,” in *Proceedings of the International Ocean Discovery Program, Lautoka, Fiji, to Papeete, 3 January–6 February 2020*.
- McKay, R. M., Naish, T., Carter, L., Riesselman, C., Dunbar, R., Sjunneskog, C., et al. (2012). Antarctic and Southern Ocean influences on late Pliocene global cooling. *Proc. Natl. Acad. Sci.* 109, 6423–6428. doi:10.1073/pnas.1112248109
- Melis, R., Capotondi, L., Torricella, F., Ferretti, P., Geniram, A., Hong, J. K., et al. (2021). Last glacial maximum to holocene paleoceanography of the northwestern Ross Sea inferred from sediment core geochemistry and micropaleontology at Hallett Ridge. *J. Micropaleontology* 40, 15–35. doi:10.5194/jm-40-15-2021
- Miramontes, E., Cattaneo, A., Jouet, G., Théreau, E., Thomas, Y., Rovere, M., et al. (2016). The pianosa contourite depositional system (northern tyrrhenian sea): drift morphology and plio-quadernary stratigraphic evolution. *Mar. Geol.* 378, 20–42. doi:10.1016/j.margeo.2015.11.004
- Miramontes, E., Garziglia, S., Sultan, N., Jouet, G., and Cattaneo, A. (2018). Morphological control of slope instability in contourites: a geotechnical approach. *Landslides* 15, 1085. doi:10.1007/s10346-018-0956-6
- Mitchell, N. C. (1993). A model for attenuation of backscatter due to sediment accumulations and its application to determine sediment thicknesses with GLORIA sidescan sonar. *J. Geophys. Res. Solid Earth* 98, 22477–22493. doi:10.1029/93jb02217
- Morrison, A. K., Hogg, A. McC., England, M. H., and Spence, P. (2020). Warm Circumpolar Deep Water transport toward Antarctica driven by local dense water export in canyons. *Sci. Adv.* 6, eaav2516. doi:10.1126/sciadv.aav2516
- Mosher, D. C., and Boggild, K. (2021). Impact of bottom currents on deep water sedimentary processes of Canada Basin, Arctic Ocean. *Earth Planet. Sci. Lett.* 569, 117067. doi:10.1016/j.epsl.2021.117067
- Neto, A. A., Mendes, J. de N. T., Souza, J. M. G. M. R., Jr, Pontes, R. L. B., and Leandro Bastos Pontes, R. (2013). Geotechnical influence on the acoustic properties of marine sediments of the santos basin, Brazil. *Mar. Georesources Geotechnol.* 31, 125–136. doi:10.1080/1064119x.2012.669815
- Ó Cofaigh, C., Dowdeswell, J. A., Allen, C. S., Hiemstra, J. F., Pudsey, C. J., Evans, J., et al. (2005). Flow dynamics and till genesis associated with a marine-based Antarctic palaeo-ice stream. *Quat. Sci. Rev.* 24, 709–740. doi:10.1016/j.quascirev.2004.10.006
- Ó Cofaigh, C., Taylor, J., Dowdeswell, J. A., and Pudsey, C. J. (2003). Palaeo-ice streams, trough mouth fans and high-latitude continental slope sedimentation. *Boreas* 32, 37–55. doi:10.1080/03009480310001858
- Ohneiser, C., Yoo, K.-C., Albot, O. B., Cortese, G., Riesselman, C., Lee, J. I., et al. (2019). Magneto-biostratigraphic age models for Pleistocene sedimentary records from the Ross Sea. *Glob. Planet. Change* 176, 36–49. doi:10.1016/j.gloplacha.2019.02.013
- Orsi, A. H., and Wiederwohl, C. L. (2009). A recount of Ross Sea waters. *Deep Sea Res. Part II Top. Stud. Oceanogr.* 56, 778–795. doi:10.1016/j.dsr2.2008.10.033
- Pérez, L. F., De Santis, L., McKay, R. M., Larter, R. D., Ash, J., Bart, P. J., et al. (2021). Early and middle Miocene ice sheet dynamics in the Ross Sea: results from integrated core-log-seismic interpretation. *GSA Bull.* 134, 348–370. doi:10.1130/B35814.1
- Pérez, L. F., Hernández-Molina, F. J., Esteban, F. D., Tassone, A., Piola, A. R., Maldonado, A., et al. (2015). Erosional and depositional contourite features at the transition between the western scotia Sea and southern south atlantic ocean: links with regional water-mass circulation since the middle Miocene. *Geo-Marine Lett.* 35, 271–288. doi:10.1007/s00367-015-0406-6
- Prothro, L. O., Majewski, W., Yokoyama, Y., Simkins, L. M., Anderson, J. B., Yamane, M., et al. (2020). Timing and pathways of East Antarctic ice sheet retreat. *Quat. Sci. Rev.* 230, 106166. doi:10.1016/j.quascirev.2020.106166
- Rebesco, M., Camerlenghi, A., Geletti, R., and Canals, M. (2006). Margin architecture reveals the transition to the modern Antarctic ice sheet ca. 3 Ma. *Geology* 34, 301–304. doi:10.1130/g22000.1
- Rebesco, M., Hernández-Molina, F. J., Van Rooij, D., and Waaahlin, A. (2014). Contourites and associated sediments controlled by deep-water circulation processes: state-of-the-art and future considerations. *Mar. Geol.* 352, 111–154. doi:10.1016/j.margeo.2014.03.011
- Rebesco, M., Larter, R. D., Camerlenghi, A., and Barker, P. F. (1996). Giant sediment drifts on the continental rise west of the Antarctic Peninsula. *Geo-Marine Lett.* 16, 65–75. doi:10.1007/bf02202600
- Rivaró, P., Frache, R., Bergamasco, A., and Hohmann, R. (2003). Dissolved oxygen, NO and PO as tracers for Ross Sea ice shelf water overflow. *Antarct. Sci.* 15, 399–404. doi:10.1017/s095410200300141x
- Rodrigues, S., Hernández-Molina, F. J., Fomes, M., Miramontes, E., Rebesco, M., and Campbell, D. C. (2022). A new classification system for mixed (turbidite-contourite) depositional systems: examples, conceptual models and diagnostic criteria for modern and ancient records. *Earth-Science Rev.* 230, 104030. doi:10.1016/j.earscirev.2022.104030
- Ryan, W. B., Carbotte, S. M., Coplan, J. O., O’Hara, S., Melkonian, A., Arko, R., et al. (2009). Global multi-resolution topography synthesis. *Geochem. Geophys. Geosystems* 10. doi:10.1029/2008gc002332
- Rydningen, T. A., Høgeth, G. V., Lasabuda, A. P. E., Laberg, J. S., Safronova, P. A., and Forwick, M. (2020). An early neogene—early quaternary contourite drift system on the SW barents Sea continental margin, Norwegian arctic. *Geochem. Geophys. Geosystems* 21, e2020GC009142. doi:10.1029/2020gc009142
- Savage, M., and Ciesielski, P. (1983). A revised history of glacial sedimentation in the Ross Sea region. *Aust. Acad. Sci. Adel.* 1983 555–559.
- Schlager, U., Jokat, W., Weigelt, E., and Gebhardt, C. (2021). Submarine landslides along the siberian termination of the lomomonosov ridge, Arctic Ocean. *Geomorphology* 382, 107679. doi:10.1016/j.geomorph.2021.107679
- Shchepetkin, A. F., and McWilliams, J. C. (2005). The regional oceanic modeling system (ROMS): a split-explicit, free-surface, topography-following-coordinate oceanic model. *Ocean. Model.* 9, 347–404. doi:10.1016/j.ocemod.2004.08.002
- Shipp, S. S., Anderson, J., and Domack, E. (1999). Late pleistocene–holocene retreat of the West antarctic ice-sheet system in the Ross Sea: part 1—geophysical results. *Geol. Soc. Am. Bull.* 111, 1486–1516. doi:10.1130/0016-7606(1999)111<1486:lphrot>2.3.co;2
- Smith, W. O., Jr., Sedwick, P. N., Arrigo, K. R., Ainley, D. G., and Orsi, A. H. (2012). The Ross Sea in a sea of change. *Oceanography* 25, 90–103. doi:10.5670/oceanog.2012.80
- Stow, D. A. (2002). *Deep-water contourite systems: modern drifts and ancient series, seismic and sedimentary characteristics*. England: Geological Society of London.
- Taylor, J., Dowdeswell, J. A., and Siegert, M. J. (2002). Late Weichselian depositional processes, fluxes, and sediment volumes on the margins of the Norwegian Sea (62–75°N). *Mar. Geol.* 188, 61–77. doi:10.1016/S0025-3227(02)00275-x
- Thompson, A. F., Stewart, A. L., Spence, P., and Heywood, K. J. (2018). The antarctic slope current in a changing climate. *Rev. Geophys.* 56, 741–770. doi:10.1029/2018rg000624

- Thran, A. C., Dutkiewicz, A., Spence, P., and Müller, R. D. (2018). Controls on the global distribution of contourite drifts: insights from an eddy-resolving ocean model. *Earth Planet. Sci. Lett.* 489, 228–240. doi:10.1016/j.epsl.2018.02.044
- Tolotti, R., Salvi, C., Salvi, G., and Bonci, M. C. (2013). Late Quaternary climate variability as recorded by micropalaeontological diatom data and geochemical data in the western Ross Sea, Antarctica. *Antarct. Sci.* 25, 804–820. doi:10.1017/S0954102013000199
- Torricella, F., Melis, R., Malinverno, E., Fontolan, G., Bussi, M., Capotondi, L., et al. (2021). Environmental and oceanographic conditions at the continental margin of the Central Basin, northwestern Ross Sea (Antarctica) since the last glacial maximum. *Geosciences* 11, 155. doi:10.3390/geosciences11040155
- Uenzelmann-Neben, G. (2006). Depositional patterns at drift 7, antarctic peninsula: along-slope versus down-slope sediment transport as indicators for oceanic currents and climatic conditions. *Mar. Geol.* 233, 49–62. doi:10.1016/j.margeo.2006.08.008
- Uenzelmann-Neben, G., and Gohl, K. (2012). Amundsen Sea sediment drifts: archives of modifications in oceanographic and climatic conditions. *Mar. Geol.* 299, 51–62. doi:10.1016/j.margeo.2011.12.007
- Uenzelmann-Neben, G. (2018). Variations in ice-sheet dynamics along the amundsen Sea and bellingshausen sea West Antarctic ice sheet margin. *GSA Bull.* 131, 479–498. Available at. doi:10.1130/B31744.1
- Veeken, P. C. H., and van Moerkerken, B. (2013). *Seismic stratigraphy and depositional facies models*. Thousand Oaks, California: EAGE publications.
- Verdicchio, G., and Trincardi, F. (2008). Mediterranean shelf-edge muddy contourites: examples from the gela and south adriatic basins. *Geo-Marine Lett.* 28, 137–151. doi:10.1007/s00367-007-0096-9
- Vorren, T. O., and Laberg, J. S. (1997). Trough mouth fans—Palaeoclimate and ice-sheet monitors. *Quat. Sci. Rev.* 16, 865–881. doi:10.1016/s0277-3791(97)00003-6
- Whitehouse, P. L., Gomez, N., King, M. A., and Wiens, D. A. (2019). Solid Earth change and the evolution of the antarctic ice sheet. *Nat. Commun.* 10, 503. doi:10.1038/s41467-018-08068-y
- Whitworth, T., III (1988). The Antarctic circumpolar current. *Oceanus* 31, 53–58.
- Wilson, D. S., and Luyendyk, B. P. (2009). West Antarctic paleotopography estimated at the Eocene-Oligocene climate transition. *Geophys. Res. Lett.* 36, L16302. doi:10.1029/2009gl039297
- Wynn, R. B., and Stow, D. A. (2002). Classification and characterisation of deep-water sediment waves. *Mar. Geol.* 192, 7–22. doi:10.1016/s0025-3227(02)00547-9